

Manuscript Number: GCA-D-18-00805

Title: Intense aqueous alteration on C-type asteroids: perspectives from giant fine-grained micrometeorites

Article Type: Article

Corresponding Author: Dr. Martin D Suttle, Ph.D

Corresponding Author's Institution: University of Pisa

First Author: Martin D Suttle, Ph.D

Order of Authors: Martin D Suttle, Ph.D; Luigi Folco, Prof.; Matthew J Genge, Dr.; Sara Russell, Prof.; Jens Najorka, Dr.; Matthias van Ginneken, Dr.

Abstract: This study explores the petrology of five giant (>400µm) hydrated fine-grained micrometeorites from the Transantarctic Mountain (TAM) micrometeorite collection. For the first time, the extent and mechanisms of aqueous alteration in unmelted cosmic dust are evaluated and quantified. We use a range of criteria, previously defined for use on hydrated chondrites, including phyllosilicate fraction, matrix geochemistry (FeO/SiO₂[wt%] vs. Mg# [At%]) and micro textures. Collectively, these micrometeorites represent ~2.22mm² of intensely altered hydrated chondritic matrix (with petrologic subtypes of <1.2 in the scheme of Howard et al., [2015]) and reveal a range of alteration styles. Two particles are found to contain pseudomorphic chondrules with thick fine-grained rims, while another micrometeorite contains several aqueously altered CAIs. Their outlines range from well-defined to indistinct, demonstrating that the advanced stages of aqueous alteration progressively remove evidence of coarse-grained components. The remaining two micrometeorites entirely lack coarse-grained components but are similarly altered. Thus, the combined chondrule-to-matrix ratio among these giant micrometeorites is extremely low (6.45%), and much below the average ratio found in typical CM or CR chondrites (~20%, Weisberg et al., 2006). Our findings are consistent with previous analyses from smaller Antarctic micrometeorites, which suggest that chondrules (and CAIs) derived from hydrated carbonaceous chondrite parent bodies are underrepresented among the micrometeorite flux, even when considering contributions from coarse-grained micrometeorites. Therefore, to explain the relative paucity of anhydrous material, we propose that the flux of fine-grained micrometeorites is primarily derived from intensely aqueously altered, primitive C-type asteroids, which have lost the majority of their refractory coarse-grained components by replacement with secondary phyllosilicate minerals.

Suggested Reviewers: Kieran T Howard
khoward@amnh.org

Has already reviewed the original submission and provided many constructive comments for improvement.

Richard Greenwood Dr.

Research Fellow, Open University

r.c.greenwood@open.ac.uk

previous studies on micrometeorites have investigated atmospheric entry and their oxygen isotope signatures.

Emmanuel Dartois Dr.

Research associate

Emmanuel.dartois@ias.u.psud.fr

Several previous publications on cometary micrometeorites and their pre-atmospheric petrography

Takaaki Noguchi Prof.

tnoguchi@artsci.kyushu-u.ac.jp

Many previous papers on asteroidal and cometary micrometeorites, with studies typically focusing on aqueous alteration

Penny Wozniakiewicz

University of Kent

P.J.Wozniakiewicz@kent.ac.uk

Previous research experience in cometary particles residues obtained from the STARDUST mission aerogel and foil craters. Current research interests include the recovery of micrometeorites from clean air by filtration methods

1 *Intense aqueous alteration on C-type asteroids: perspectives from giant fine-grained*
2 *micrometeorites* [GCA-D-18-00240]

3 Suttle, M.D.^{1,2,3}(*corresponding author*), Folco, L.¹, Genge, M.J.^{2,3}, Russell, S.S.³, Najorka, J.³, van
4 Ginneken, M.^{4,5,6}. – martindavid.suttle@dst.unipi.it, luigi.folco@unipi.it, m.genge@ic.ac.uk,
5 sara.russell@nhm.ac.uk, j.najorka@nhm.ac.uk, matthias.van.ginneken@ulb.ac.be

7 ¹Dipartimento di Scienze della Terra, Università di Pisa, 56126 Pisa, Italy

8 ²Department of Earth Science and Engineering, Imperial College London, South Kensington, London, SW7 2AZ,
9 UK

10 ³Core research laboratories, Department of Earth Science, The Natural History Museum, Cromwell Rd, London
11 SW7 5BD, UK

12 ⁴Analytical and Environmental Chemistry (ANCH), Vrije Universiteit Brussel, Av. F.D. Roosevelt 50, 1050
13 Brussel, Belgium.

14 ⁵Laboratoire G-Time, Université Libre de Bruxelles, Franklin Rooseveltlaan 50, 1050 Bruxelles, Belgium

15 ⁶Royal Belgian Institute of Natural Sciences, Rue Vautier 29, 1000 Bruxelles, Belgium

17 **Abstract**

18 This study explores the petrology of five giant (>400 μ m) hydrated fine-grained micrometeorites from
19 the Transantarctic Mountain (TAM) micrometeorite collection. For the first time, the extent and
20 mechanisms of aqueous alteration in unmelted cosmic dust are evaluated and quantified. We use a
21 range of criteria, previously defined for use on hydrated chondrites, including phyllosilicate fraction,
22 matrix geochemistry (FeO/SiO₂[wt%] vs. Mg# [At%]) and micro textures. Collectively, these
23 micrometeorites represent ~2.22mm² of intensely altered hydrated chondritic matrix (with petrologic
24 subtypes of <1.2 in the scheme of Howard et al., [2015]) and reveal a range of alteration styles. Two
25 particles are found to contain pseudomorphic chondrules with thick fine-grained rims, while another
26 micrometeorite contains several aqueously altered CAIs. Their outlines range from well-defined to
27 indistinct, demonstrating that the advanced stages of aqueous alteration progressively remove
28 evidence of coarse-grained components. The remaining two micrometeorites entirely lack coarse-
29 grained components but are similarly altered. Thus, the combined chondrule-to-matrix ratio among
30 these giant micrometeorites is extremely low (6.45%), and significantly below the average ratio found
31 in typical CM or CR chondrites (~20%, Weisberg et al., 2006). Our findings are consistent with previous
32 analyses from smaller Antarctic micrometeorites, which suggest that chondrules (and CAIs) derived
33 from hydrated carbonaceous chondrite parent bodies are underrepresented among the
34 micrometeorite flux, even when considering contributions from coarse-grained micrometeorites.
35 Therefore, to explain the relative paucity of anhydrous material, we propose that the flux of fine-
36 grained micrometeorites is primarily derived from intensely aqueously altered, primitive C-type
37 asteroids, which have lost the majority of their refractory coarse-grained components by replacement
38 with secondary phyllosilicate minerals.

39 1. Introduction

40 The interaction between liquid water and solid nebular condensates is termed aqueous alteration and
41 represents a critical process of the early solar system's evolution. Alteration known to have occurred
42 independently on numerous small bodies (Trigo-Rodriguez et al., 2006; Elmaleh et al., 2015) and
43 potentially, even within the nebular itself, where grain aggregates, containing water-ice, were heated
44 by the Sun, from passing shock waves or by other transient mechanisms (Metzler et al., 1992; Ciesla
45 et al., 2003).

46 Most primitive extraterrestrial materials, including ordinary chondrites (Doyle et al., 2015),
47 carbonaceous chondrites (Rubin et al., 2007; Harju et al., 2014; King et al., 2015), micrometeorites
48 (Genge et al., 1997; Suttle et al., 2017a), interplanetary dust particles (Rietmeijer, 1991) and cometary
49 dust (Zolensky et al., 2006; Noguchi et al., 2017) show evidence of aqueous alteration. However, this
50 is most advanced, and most extensively studied, among the hydrated carbonaceous chondrite group
51 (containing the CM and CI chondrites as well as a significant fraction [~70%, Harju et al., 2014] of the
52 CR chondrites). These meteorites are dominated by secondary minerals, formed during alteration and
53 contain between 2 and 20wt% water (Tonui et al., 2003; Rubin et al., 2007), primarily this is structural
54 water held inside hydrated phyllosilicate minerals. Both the CM and CI chondrites are dominated by a
55 complex, mixed assemblage of interlocking Fe and Mg-phyllosilicate (Tomeoka and Buseck, 1985;
56 Browning et al., 1996), representing multiple generations of secondary mineral growth (Elmaleh et al.,
57 2015; Lee et al., 2012; 2013). They also contain accessory Fe-Mg-Ca carbonates, minor Fe-oxides and
58 dispersed hydrated Fe-Ni sulfides (Weisberg et al., 2006; Howard et al., 2009; 2015; King et al., 2015).
59 Relict, anhydrous mafic silicate crystals (typically Mg-rich olivine and pyroxene grains) may be
60 preserved, commonly as isolated matrix grains or grain clusters, representing the incompletely
61 transformed remnants of chondrules, CAIs (Ca-Al inclusions) and AOAs (amoeboid olivine aggregates)
62 (Hanowski et al., 2001; Velbel et al., 2012; Pignatelli et al., 2016).

63 In addition to disequilibrium mineral assemblages and complex alteration chronologies, the extent of
64 aqueous alteration among the hydrated chondrite population is highly variable (Rubin et al., 2007;
65 Harju et al., 2014; Howard et al., 2015). In general, CI chondrites are more extensively altered and are
66 composed almost entirely of hydrated fine-grained matrix (King et al., 2015), while most CM
67 chondrites are less-altered and retain some anhydrous components (between 5-32 vol% and typically
68 around 25 vol%, Howard et al., 2009; 2015). However, increasingly a population of extensively altered
69 CM chondrites, with alteration degrees equivalent to their CI counterparts are being described and
70 classified (Zolensky et al., 1996; 1997; Rubin et al., 2007; King et al., 2017). In contrast, most CR
71 chondrites are less-altered than either the CM or CI groups (Howard et al., 2015) and, therefore,
72 preserve the early stages of aqueous alteration in chondritic materials (Harju et al., 2014; Le Guillou
73 et al., 2015). Variations in the extent of aqueous alteration are also observed within individual
74 meteorites (Zolensky et al., 1997; Lee et al., 2013). This may be due to impact brecciation on the parent
75 asteroid (Zolensky et al., 2014) but also reveals that interaction with liquid water was localized and
76 potentially short lived (Weisberg and Huber, 2007; Bland et al., 2009; Lee and Lindgren, 2016).

77 **1.1. Evaluating the extent of aqueous alteration in carbonaceous chondrites** – Attempts to
78 characterise the style, extent and mechanisms of aqueous alteration in hydrated chondrites have used
79 a range of petrographic criteria including: textural features (Velbel et al., 2012; Lee and Lindgren,

80 2016), elemental ratios (McSween 1979; 1989; Rubin et al., 2007), modal mineralogy (Howard et al.,
81 2009; King et al., 2017), spectroscopy (Takir et al., 2013) and isotopic signatures within various mineral
82 phases – notably carbonates (Lee et al., 2012; 2013). This led to the development of several different
83 aqueous alteration schemes that assign a petrologic subtype (a numerical designation) to individual
84 meteorites, defining their degree of alteration – where lower subtypes represent more intensely
85 altered samples.

86 The main effect of aqueous alteration is the progressive replacement of a parent body's primary
87 lithology with secondary minerals. Thus, most alteration metrics attempt to measure the relative
88 amount of replacement that has occurred within a meteorite. Geochemical metrics, which measure
89 the composition of the fine-grained matrix trace changes in the composition of the alteration fluid as
90 new secondary minerals are precipitated. McSween (1979; 1987) noted that as alteration advances,
91 Fe/Si ratios decrease, while Mg/Fe ratios increase. This trend reflects the progressive loss of Mg-rich
92 anhydrous silicates (olivine and pyroxene), whose subsequent donation of Mg into the fluid phase
93 results in the precipitation of increasingly Mg-rich phyllosilicates (Browning et al., 1996; Howard et al.,
94 2009) and later Mg-rich carbonates (Lee et al., 2014). Texturally, this corresponds to the loss of coarse-
95 grained structural elements within the meteorite, first as chondrule glass is replaced, and later as
96 chondrule minerals, CAIs (Ca-Al-rich inclusions), AOAs (amoeboid olivine aggregates) and isolated
97 matrix silicates are converted into phyllosilicate (Zolensky et al., 1997; Rubin et al., 2007; Velbel et al.,
98 2012; Lee and Lindgren, 2016). Alteration, therefore, has the effect of homogenising the chondrite,
99 both texturally and geochemically. From a mineralogical perspective, the degree of aqueous alteration
100 can be tracked and quantified simply by measuring the phyllosilicate fraction (calculated as: [total
101 phyllosilicate/[total phyllosilicate + total anhydrous silicate]]) within a sample. Although this is a
102 relatively crude indicator of alteration extent – which lacks the high-fidelity precision achievable with
103 other methods, such as isotopy (Lee et al., 2014; Lee and Lindgren, 2016) or through the combined
104 use of several different metric as in Rubin et al., (2007) – it is possible, using only the phyllosilicate
105 fraction, to compare the degree of alteration between hydrated chondrites within the CM and CR
106 chondrite groups as well as the C2 ungrouped meteorites (Howard et al. 2015).

107 **1.2. Comparative studies on fine-grained micrometeorites** – Many studies have revealed strong
108 geochemical, mineralogical, textural and isotopic affinities between micrometeorites and hydrated
109 carbonaceous chondrites. For example, Alexander et al., (2002), Genge et al. (1997) and Taylor et al.,
110 (2012) each demonstrated that the bulk compositions of most fine-grained micrometeorites show a
111 close relationship to that of CM chondrites, while Kurat et al., (1991) and van Ginneken et al. (2012)
112 matched the mineralogy and trace element geochemistry of several large chondritic micrometeorites
113 to known meteorite groups, including CM and CI chondrites. Furthermore, Suavet et al. (2010)
114 analysed oxygen isotopes in large (>500µm) particles and revealed that the majority (~50%) of these
115 micrometeorites have signatures which directly relate them to the joint CM-CR isotopic group.

116 Alternatively, micrometeorites may originate from parent bodies which are related to, but distinct
117 from the established CM/CR/CI carbonaceous chondrite groups. This argument is supported by subtle
118 differences between the two groups, including: an apparent lack of chondrules among the fine-grained
119 micrometeorite population (Engrand and Maurette, 1997; Reshma et al., 2013), higher
120 olivine/pyroxene ratios in micrometeorites than chondrites, as well as a lack of carbonate and sulfate
121 phases (Kurat et al., 1994). Micrometeorites also have unique organic signatures, containing higher

122 CH₂/CH₃ ratios and lower carbonyl abundances than chondrites (Battandier et al., 2018) as well as
123 trace element compositions of their olivine and pyroxene grains which extend outside the
124 compositional ranges observed for silicates in established carbonaceous chondrite groups (Steele,
125 1992).

126 Although aqueous alteration has been extensively researched within the hydrated chondrites,
127 comparable studies focusing on the extent of aqueous alteration in fine-grained micrometeorites are
128 notably absent and this limits our ability to confidently answer the question: do fine-grained
129 micrometeorites originate from the same parent bodies as CM, CR and CI chondrites, or are
130 micrometeorites sourced from distinct parent asteroids? The absence of studies investigating aqueous
131 alteration in fine-grained micrometeorites is most likely a product of two main limitations:
132

133 (1) **The small size of micrometeorites** – which are typically <200µm (Taylor et al., 2000) and always
134 <3000µm (Suavet et al., 2009) – this means that all micrometeorites will be unrepresentative samples
135 of their parent body’s geology (Genge et al., 2008). The minimum size necessary for a representative
136 sampling of coarse-grained components in chondritic material was quantified by Hezel et al., (2008),
137 who calculated that extremely large surface areas, >2500mm², are needed. Thus, all micrometeorites
138 and most small meteorite chips suffer sampling biases. Although, this problem is inherent in any study
139 of micrometeorites, sampling bias may be partially overcome either through the analysis of many
140 individual particles, or where larger samples, which are significantly more representative than their
141 smaller counterparts are studied.

142 Here, we provide the first data on aqueous alteration in giant fine-grained micrometeorites, whose
143 exposed surface areas (0.21-1.15mm²) are sufficiently that coarse-grained structural components,
144 such as CAIs, AOAs and chondrules are expected to be found. However, despite their larger size, the
145 conclusions drawn from these micrometeorites should be considered along with existing data from
146 small micrometeorites and larger hydrated carbonaceous chondrites, thereby providing a more
147 comprehensive view of the flux of hydrated chondritic material to Earth.

148 (2) **The effects of terrestrial overprints**, including atmospheric entry heating and terrestrial
149 weathering also overprint a particle’s parent body petrography. Flash heating during atmospheric
150 entry significantly alters the mineralogy and textures of most micrometeorites (Suttle et al., 2017a).
151 Even among unmelted micrometeorites, the hydrated phyllosilicate matrix has typically experienced
152 dehydration, dehydroxylation or recrystallization at sub-solidus temperatures during entry.
153 Meanwhile, at the micrometeorite’s margin, localized melting and degassing occurs resulting in the
154 formation of igneous and magnetite rims (Genge, 2006) and, in extreme cases, particle fragmentation
155 (Suttle et al., 2018). By contrast, terrestrial weathering leads to leaching, dissolution and replacement
156 of parent body minerals with hydrated, S, K and Cl-rich phases, such as jarosite and halite and calcite
157 (van Ginneken et al., 2016). The effects of these later geological processes must be understood before
158 a sample’s parent body geology can be analysed.

159 In this study, we characterise the petrography of five giant fine-grained micrometeorites and evaluate
160 their degree of aqueous alteration. This provides new data on the relationship between
161 micrometeorites and known carbonaceous chondrite groups, whilst also expanding the discussion of
162 aqueous alteration on primitive C-type asteroids to include perspectives from the micrometeorite flux.

163 This study therefore complements existing studies based on smaller (<100µm) micrometeorites and
164 their larger C2/C1 hydrated meteorite counterparts.

165 **2. Samples**

166 Micrometeorites recovered from loose sediments on the summit plateaus of the Transantarctic
167 Mountains represent a unique collection of cosmic dust, characterised by abundant large (>500µm)
168 micrometeorites (Suavet et al., 2009). This contrasts with the size distributions from all other
169 Antarctic, deep-sea and fossil micrometeorite collections that are dominated by small particles
170 (<600µm and typically <150µm, Taylor et al., 2000; Suavet et al., 2009; Suttle et al., 2017b). The
171 advantage of studying such large micrometeorites, lies in the ability to analyse a more representative
172 sample of their parent asteroid and, therefore, to draw more reliable conclusions about the
173 provenance and geological history of individual particles.

174 The estimated total accumulation duration for the TAM micrometeorite collection lies between 1-
175 3Ma. This is constrained by the presence of Australasian microtektites, with a formation age of
176 ~0.78Ma (Folco et al., 2008), by the presence of cosmic spherules with a thermal remnant
177 magnetization signature acquired during the Earth's reversed polarity field, also >0.78Ma ago (Suavet
178 et al., 2011), and from ¹⁰Be, bedrock exposure ages, measured on the terrestrial collection surface
179 (~4.4Ma, Welten et al., 2008). Such long time periods are necessary for the accumulation of rare, large
180 micrometeorites (Suavet et al., 2009). However, long residence times exposed above the ice sheets,
181 have also resulted in significant terrestrial weathering (van Ginneken et al., 2016; Genge et al., 2018).
182 Consequently, most TAM micrometeorites have encrustations and secondary replacement with
183 jarosite, calcite and halite minerals, which progressively overprint their parent body and atmospheric
184 signatures (van Ginneken et al., 2016).

185 We selected five of the largest, fine-grained micrometeorites (460-1000µm, TAM19B-7, TAM19B-17,
186 TAM19B-18, TAM15-11 and TAM66-1) which were obtained from sediment traps, located on the
187 nunatak Miller Butte [72°42.078' S, 160°14.333' E, at an elevation of ~2600m]. Some of these particles
188 were previously analysed in two previous publications by Suttle et al., (2017a; 2018), which focused
189 on the petrographic evolution of fine-grained micrometeoroids during atmospheric entry heating.
190 However, in this study we, instead, investigate the pre-atmospheric, parent body properties of these
191 samples, specifically looking at aqueous alteration on their parent asteroids.

192 **3. Methods**

193 Our micrometeorites were analysed primarily at the Natural History Museum (NHM), London in the
194 Imaging and Analysis Centre. Particles were investigated using a range of microanalysis techniques,
195 including: back-scatter electron imaging (BEI), electron microprobe analysis (WD-EMPA), standard-
196 based SEM-EDS, elemental X-ray mapping and micro X-ray diffraction (µXRD). Later, at the University
197 of Pisa, Italy we also collected high-resolution BEI and standard-less EDS data on two particles: TAM66-
198 1 and fragments from TAM19B-7. Table.1 displays the analysis types performed on each sample.

199 For a single particle, TAM19B-7, we also conducted a petrofabrics analysis to investigate the
200 relationship between aqueous alteration and shock deformation. After which we extracted TAM19B-
201 7 from the epoxy resin, crushed the particle and re-embedded 10 fragments (~50-300µm in size) for
202 further analysis. In addition, we have preserved the remaining particle's mass (~0.5mg) for a planned
203 future O-isotope study. By fragmenting this micrometeorite and analysing several random chips we

204 are able to explore significantly more of the particle's petrography and, therefore, achieve a more
205 representative analysis of the micrometeorite.

206 **3.1 Geochemistry and mineralogy** – Geochemical data were collected using either a Cameca SX100
207 SEM – a WD-EMPA system, a Zeiss SEM-EVO 15LS fitted with an Oxford Instruments' 80mm² X-Max
208 silicon drift detector (SSD) energy dispersive spectrometer (EDS), providing standard-based
209 geochemical assays or a FEI Quanta 450 field emission SEM, equipped with a Bruker Quantax 400
210 XFlash detector [with a 129eV spectral resolution], which provided standard-less EDS data.

211 For the Cameca, WDS analyses were performed under acceleration voltages of 20kV, beam currents
212 of 10nA and a focused beam spot (<1µm diameter). The system was calibrated, prior to use, with a
213 suite of mineral standards, specific to each element under detection. Eleven elements, commonly
214 found in silicate minerals were included in the pre-defined element list, with oxygen calculated by
215 stoichiometry. After analysis, the in-house Cameca PAP matrix correction software was used to
216 remove artefacts arising from atomic number, absorption and secondary fluorescence effects.
217 Elemental detection limits for this instrument are on the order of 0.02-0.05wt% and elemental
218 uncertainties vary between 0.01-0.03wt%.

219 For the standard-based EDS system [Zeiss EVO], data were collected under acceleration voltages of
220 20kV, beam currents of 3nA and a focused beam spot (~1µm diameter). Pre-analysis gain calibrations
221 were performed on an elemental cobalt standard, while routine monitoring of beam current, count
222 deadtimes, acceleration voltages and sample-detector distance ensured ideal conditions were
223 maintained throughout data collection. Post-acquisition processing used the Oxford Instruments INCA
224 software. Weight totals were calculated using "oxygen by stoichiometry" which assumes that all
225 cations occupy their lowest oxidation states. Elemental detection limits are on the order of 0.2wt%
226 and analytical uncertainties vary between 0.1-0.5wt%.

227 A FEI Quanta 650 FEG-SEM, located at the NHM and fitted with a Bruker Flat Quad 5060F EDS detector
228 plate was used to collect BEI data as well as high spatial resolution quantitative X-ray element maps.
229 These were generated using a 12kV beam which rastered over the micrometeorite cross-sections for
230 2-24hours. Count rate of 27.7kcps and deadtimes between 5-10% were maintained throughout
231 acquisition.

232 A Rigaku Rapid II micro-diffraction system, containing a 2D curved imaging plate detector, a Cu X-ray
233 source, a collimator pinhole system and adjustable goniometer head were employed to collect
234 diffraction data. A 100µm beam spot was used and samples ran for approximately 20 hours, during
235 this time the micrometeorite cross section, embedded in epoxy resin, were held at a constant ω angle
236 (2θ) but continuously rotated in the ϕ axis. Peak positions in the converted 1D patterns were
237 identified by comparison against a comprehensive mineral standards database (PDF-4 database from
238 ICDD).

239 More detailed information for each of the analytical procedures and their operating conditions can be
240 found in Suttle et al., (2017a; 2018).

241 **3.2. 2D shock fabric analysis** – All five micrometeorites were analysed with a 2D image analysis
242 procedure, that evaluates the orientations of void space within a fine-grained micrometeorite's
243 matrix. This was investigated by extracting and measuring the area and direction of each void's long-
244 axis with respect to an arbitrary reference 'north'. The minimum void size analysed was set at a
245 threshold of 50µm². Smaller voids were ignored since these were composed of relatively few pixels.

246 Void orientations were binned by 10° increments and used to generate circular histograms (rose
247 diagrams) from which the presence or absence of a petrofabric could be determined. Rose diagrams
248 were evaluated quantitatively using entropy calculations to determine the degree of disorder. A lower
249 entropy value reflects a mature fabric with a well-defined alignment of voids, while randomly
250 orientated voids generate an isotropic (uniform circular) rose diagram and, therefore, a high entropy.
251 Additional details of this data processing procedure can be found in Suttle et al., (2017b) whose
252 technique was followed in this study. In addition, the entropy values of the CM chondrites (Cold
253 Bokkeveld and Jbilet Winselwan) also analysed in Suttle et al., (2017b) are employed in this study to
254 provide context to the entropy value calculated from the giant TAM micrometeorites.

255 **4. Results**

256 **4.1. General characteristics** – All five particles have characteristic textural and petrographic features
257 that identify them as unmelted, fine-grained micrometeorites. These include partial or complete
258 magnetite rims, igneous rims, vesicles, Ni-bearing forsterite (seen in 4 of 5 particles), abundant Mg
259 and Fe-bearing phyllosilicate, in the form of intergrown clusters or clumps (which are now seen as
260 amorphous dehydration products and identified by the presence of dehydration cracks) and accessory
261 Fe-Ni metal and Fe-oxides (Figs.1-5 in this manuscript may be compared with micrometeorites shown
262 in Genge et al. [2008]).

263 The TAM micrometeorites also have similar compositions (Figs.6 and 7, Table.2), characterised by
264 chondritic abundances for Al, Ti, Si, V, Cr, P, Mn, Cu, Na and S and depletions, up to 1 order of
265 magnitude below CI Ivuna, for Ca, Mg, Ni, Co and Zn. In the case of Mg, depletions vary between 0.16-
266 0.61x below CI values. Conversely, mild enrichments are seen for Fe, between 1.4-2.2x, while all
267 micrometeorites also contain significantly elevated K concentrations (>10.9x), which in TAM51.11
268 reach up to 35x CI values. Deviations from chondritic concentrations are primarily a product of
269 terrestrial weathering, where long residence times in the Antarctic environment have resulted in the
270 leaching and dissolution of soluble phases, the alteration of glass and the formation of secondary
271 minerals such as jarosite, akaganéite, palagonite, (Mg,Fe)-oxyhydroxides, calcite and halite (van
272 Ginneken et al., 2016). Terrestrial alteration by jarosite replacement is common in the TAM
273 micrometeorites and forms thick encrustation rims, which are notable on TAM19B-17 (Fig.2).
274 Akaganéite was also identified as a major phase in the μ XRD pattern of TAM19B-7 (Fig.7). This mineral
275 forms where FeNi-sulfides (pyrrhotite, troilite and tochilinite) are altered in the presence of Cl-bearing
276 water and is, therefore, a common component of weathered Antarctic meteorites (Bland et al., 1997).

277 **4.2. TAM19B-7**

278 **4.2.1. Main cross-section** – This particle is the largest unmelted, fine-grained micrometeorite analysed
279 to date. The main cross-sectioned surface (Fig.1A-D) has a rectangular shape, with dimensions of
280 $\sim 830 \times 950 \mu\text{m}$ and an exposed surface area of 0.69mm^2 . The particle's matrix is highly vesicular,
281 suggesting that this micrometeorite is transitional between the fine-grained and scoriaceous class,
282 thereby reflecting the effects of partial melting during atmospheric entry. However, relict textures
283 show that the pre-atmospheric matrix was compact, dense and fine-grained, being composed of
284 phyllosilicates (with a high phyllosilicate fraction of 0.97) and with minimal coarse-grained PCP clumps.
285 The most distinctive feature of this particle is the presence of two geochemically distinct domains,
286 separated by a relatively sharp compositional contact (with a boundary thickness of $\sim 5 \mu\text{m}$). The lower
287 left portion of the micrometeorite contains Mg at concentrations between 4.1-8.2wt% and Fe at

288 concentrations between 12.4-20.9wt%, while the upper right domain is heavily depleted in Mg, with
289 concentrations below 3.0wt%. However, Fe concentrations in this region is high, varying between
290 16.0wt% and 31.9wt%. These two domains are, therefore, Mg-bearing (Mg#26-60) and Fe-rich (Mg#0-
291 36) respectively. In the upper right portion, the majority of large voids (vesicles, dehydration cracks
292 and interconnected networks formed from both void types [Suttle et al., 2018]) have Fe-rich linings,
293 while Fe-rich linings are less pronounced in the Mg-bearing domain.

294 Within the Fe-rich domain there is a rounded elliptical region of matrix with dimensions of
295 approximately 180x140 μm and an average diameter of $\sim 160\mu\text{m}$ (Fig.1B, aspect ratio of ~ 1.3). This
296 component is geochemically indistinguishable from the host micrometeorite, but clearly identifiable
297 under BEI due to its distinctive matrix texture. This object is mantled by a fine-grained, weakly layered
298 and compact rim with variable thickness, between 10-25 μm . The inclusion core has an abundance of
299 rounded voids (<20 μm diameter), which results in a high porosity. Several of these voids are coated
300 with Fe-rich rims (Suttle et al., 2018).

301 **4.2.2 Additional fragments** – We subsequently crushed TAM19B-7 and analysed the resulting
302 fragments (some of which are shown in Fig.1E-H). The exposed cross-sectional areas of these
303 fragments are smaller, ranging from 0.01-0.12 mm^2 . However, these chips effectively increase the total
304 area of analysis by 40% and provide a 3D perspective of the particle interior. Two of the fragments
305 shown in Fig.1 (E and H) are orientated at 90° to the original cross-section (shown in Fig.1A-D) and
306 include the flat, polished surface of the initial section on one edge – these are marked by a dashed
307 green line. Despite increasing the area for analysis, we did not find additional unambiguous coarse-
308 grained components, although two fragments (Fig.1G and 1H) with faint rounded outlines were
309 observed and these may represent additional inclusions.

310 **4.3. TAM19B-17** – This micrometeorite has a triangular cross-section, with maximum dimensions of
311 460x480 μm and a total exposed surface area of 0.21 mm^2 (Fig.2A.). The phyllosilicate matrix is
312 heterogenous, fine-grained, Fe-rich (avg Mg#18) and dense, containing limited pore space. Significant
313 variations in back scatter potential (between Mg#3-38) produce a complex texture of intergrown or
314 amorphous phases. For example, dark, poorly defined and dense regions of relatively Mg-rich matrix
315 (Mg>6wt%) are sparse and mantled or cross-cut by large clusters of lighter, Fe-enriched (Mg<3wt%,
316 Fe>20wt%) and coarser-grain material, which may contain several small dehydration cracks. The
317 calculated phyllosilicate fraction for this micrometeorite is 0.96. Micron scale veins and infilled pores
318 are also identified (Fig.2E).

319 Anhydrous silicates in TAM19B-17 are relatively common and appear as large (>80x100 μm) forsterite
320 crystal clusters with anhedral morphologies. Grains may enclose small (<4 μm diameter) Fe-Ni metal
321 droplets or are surrounded by thin (<5 μm) Fe-Ni sulfide linings. Most silicate crystals are heavily
322 altered and replaced, as evidenced by their rounded outlines (Fig.2E). Several grains have broken into
323 a series of smaller residual silicate crystals or contain fractures. Silicate margins are also surrounded
324 by thick (>20 μm) Fe-rich growths. In Fig.2A the outlines of three prominent refractory crystal clusters
325 have been traced. They have rounded, elongate and oval-shaped morphologies. These regions
326 typically have darker greyscale colours (low Z values) representing Mg-enriched matrix in between the
327 crystal fragments.

328 TAM19B-17 also has several combined Ca, Al and Ti hotspots (Fig.2C). Four such zones of enrichment
329 are identified, the largest of which is shown in Fig.2D and exceeds 100 μm in diameter. The core of this

330 hotspot contains small Al-spinels embedded within a porous material, which we tentatively identify
331 as bridgmanite - a silicate perovskite composed of ferromagnesian silicates [(Mg,Fe)SiO₃] and calcium
332 silicate [wollastonite, CaSiO₃], and whose combined stoichiometry approaches (Mg,Fe,Ca)(Al,Si)O₃
333 (Table.2, B1-3). This core of this inclusion is surrounded by a thick and equally porous margin of more
334 Fe-enriched material with a stoichiometry closer to that of an Al-rich pyroxene.

335 **4.4. TAM19B-18** – This micrometeorite has an elongated and irregular cross-section, with dimensions
336 of 870x530µm and a total exposed surface area of 0.27mm² (Fig.3A). The particle is dominated by
337 large (>80µm) clusters of coarse, Fe-rich phyllosilicates (Mg#20-44, ~3-9wt% Mg) which are identified
338 by their prominent internal and subparallel dehydration crack sets (Fig.3E and F) and relatively sharp
339 compositional boundaries. These coarse phyllosilicate clumps represent up to 85% of the particle's
340 exposed surface area, giving this particle a high calculated phyllosilicate fraction of 0.93. The
341 remaining regions, seen in cross-section, are either pore space, which is primarily in the form of large
342 and interconnected cracks (Suttle et al., 2018), or isolated anhydrous silicates (Fig.3B, C and E). The
343 compositions of olivine crystals varies between Fo22-98 and in size between ~<5-120µm. Most silicate
344 grains contain penetrating fractures that are infilled by thin serpentine veins (Fig.3C). Thick
345 phyllosilicate mantles also wrap around most crystals (Fig.3B), producing overgrowth rims that have a
346 weakly foliated texture.

347 This micrometeorite also contains an embedded clast (~130x180µm, Fig.3A) characterised by a
348 compact, mildly Mg-enriched matrix (Mg#39-49, ~7-9wt% Mg) and contains a single large (35x40µm)
349 olivine crystal. Sub-spherical micron-scale Fe-oxide beads are also present in the matrix, prior to
350 atmospheric entry, these were most likely tochilinite grains or Fe-oxides.

351 **4.5. TAM15-11** – This micrometeorite has an irregular, broadly triangular cross-section with
352 dimensions of approximately 1000x470µm and a total exposed surface area of ~0.30mm² (Fig.4A). The
353 particle margin has a well-developed but discontinuous magnetite rim and localised portions of
354 igneous rim. Meanwhile, the particle interior is primarily composed of (dehydroxylated) coarse-
355 grained Fe-rich (Mg# 2-46%, 0.2-8.3wt% Mg) phyllosilicate clusters (Fig.4A and 4E), which contain
356 large sub-parallel dehydration crack sets and finer-grained Mg-enriched zones (Fig.4G). The coarse
357 phyllosilicate clusters have irregular, elongated or lozenge shapes and reach up to ~300µm in length.
358 Anhydrous silicate crystals range in size from <5µm (Fig.4D) to 80µm (Fig.4C) and compose
359 approximately 1.5% of the particle's exposed surface area (resulting in an extremely high phyllosilicate
360 fraction of 0.98). Most of the anhydrous silicates are pyroxenes, with both low-Ca pyroxene (En93-96,
361 Fs2-5, Wo0-1 [as enstatite]) and high-Ca pyroxene (En49-56, Fs2-5, Wo39-46 [reflecting both augite
362 and diopside compositions]) being common and occurring in close association (Fig.4C). By contrast,
363 olivine is relatively rare and has a Mg-poor composition (Fo46). The anhydrous silicate crystals are
364 collected into discrete clusters and have either sharp fractured margins and angular morphologies
365 (Fig.4C) or smooth and rounded edges which show a distinct Fe-enrichment (Fig.4D).

366 **4.6. TAM66-1** – This micrometeorite has a smooth fine-grained external surface (Fig.5G) and
367 dimensions of 1000x950x720µm. In cross-section, the exposed surface area is approximately
368 930x740µm, equivalent to ~0.29mm² (Fig.5A). The particle margin supports a well-developed but
369 discontinuous magnetite and igneous rim, which is broken in several places along the top and right
370 sides (Fig.5A). These fractures are assumed to form whilst on the Earth's surface as a result of
371 weathering and transport. Fractures also cut through the particle interior, following the margins of

372 inclusions (Fig.5C and F) and the boundaries between larger anhydrous silicate crystals and fine-
373 grained matrix, as shown in Fig.5E.

374 The micrometeorite's interior contains several distinct regions of fine-grained Fe-poor/Si-rich matrix
375 which are surrounded by thick mantles of (dehydroxylated) Fe-rich phyllosilicate with a vesicular
376 texture. This is demonstrated in Fig.5C and 5F, where two approximately circular inclusions, with
377 dimensions of 280x200 μm and 90x80 μm respectively are present. They both have thick rims with
378 variable widths (40-100 μm and 30-40 μm respectively), while the inclusion cores contain a compact
379 zone composed of Mg-depleted (1.5-3.4wt%, $\sim\text{Mg}\#10\text{-}30$) dark matrix which has several small (5-
380 15 μm) rounded, residual anhydrous silicate crystals, with predominantly low-Ca pyroxene
381 compositions (En60-66, Fs34-38, Wo<2). Likewise, the remainder of the particle's matrix is also
382 composed of many small isolated regions with irregular shapes and well-defined margins. They have
383 similar textural relationships defined by vesiculated Fe-rich matrix mantling residual anhydrous silicate
384 crystals, as shown in Fig.5E – where a single Low-Ca pyroxene grain has been surrounded and partially
385 infilled with phyllosilicate matrix or as in Fig.5D – where a region of dark matrix, containing high-Ca
386 pyroxene is similarly enclosed.

387 **4.7. Petrofabric analyses** – The 2D image processing technique outlined in Suttle et al., (2017c) was
388 used to evaluate the orientation of voids within the matrix of all five micrometeorites (Fig.9 and
389 Table.3). Low entropy values ($S < 2.783$ [jbilet Winselwan]), low circular variance values ($\sigma^2 < 0.3$) and
390 high kappa concentration factors ($\kappa > 0.5$) indicate a well-defined preferred orientation of their internal
391 voids and consequently strong petrofabrics, defined by the former existence of aligned phyllosilicates
392 (Suttle et al., 2017c).

393 Two micrometeorites (TAM19B-7 [$S=2.599$] and TAM19B-17 [$S=2.688$]) fit these criteria. TAM19B-7
394 demonstrates the strongest alignment of void long-axes, which trend in an NW-SE orientation; this is
395 broadly parallel to the flattening direction of the elliptical inclusion seen in Fig.1B. In contrast, the
396 petrofabric in TAM19B-17 was calculated from only 48 voids, rather than several hundred, as with the
397 other samples. Thus, due to the lower porosity of this micrometeorite, the petrofabric analysis carries
398 a significantly lower degree of certainty. Two further micrometeorites (TAM15-11 [$S=2.744$] and
399 TAM19B-18 [$S=2.785$]) have relatively low entropy values similar to the two shocked CM chondrite
400 reference samples and, therefore, weaker petrofabrics, which we have defined as probable and
401 possible respectively. In contrast, no preferred orientation of voids was detected in TAM66-1
402 [$S=2.860$].

403 **5. Discussion**

404 **5.1. Separating terrestrial weathering from parent body features** – On Earth, micrometeorites are
405 attacked from the particle edge as terrestrial alteration migrates inwards. Because the TAM collection
406 is the focus of the only dedicated study into the mechanics of weathering in micrometeorites (van
407 Ginneken et al., 2016), their distinctive weathering profiles; formed in cold, acidic and subaerial
408 environments are well-documented. As previously outlined, jarosite, halite and calcite typically form
409 additions to particles as thick encrustations coating particle exteriors. Simultaneously, micrometeorite
410 interiors are slowly replaced by simple weathering products, including jarosite, akaganéite,
411 palagonite, ferrihydrite, limonite and Al-bearing clay minerals. Here, the leaching of fluid-mobile
412 elements commonly occurs, with the loss of Ni, Co, S being common effects. Moreover, in heavily
413 leached particles Mg depletions occur (Kurat et al., 1994; Genge et al., 1997). Similarly, anhydrous

414 silicates are etched by acids and dissolved leaving cavities which are later infilled. Similarly, voids such
415 as cracks and vesicles are also progressively infilled.

416 Although the five micrometeorites studied here have significant weathering overprints, both
417 geochemical (Figs.6 & 7) and textural (Fig.1-5, particle margins) their pre-atmospheric parent body
418 textures and much of their geochemistry is well-preserved and resolvable. This is evident from the
419 retention of broadly chondritic compositions, the preservation of subtle matrix textures, including the
420 elliptical inclusions seen in TAM19B-7 and TAM66-1 (Figs.1B, 1C, 5C and 5F) and the overgrown
421 phyllosilicate clusters in TAM19B-18 (Fig.3A) and TAM15-11 (Fig.4A and E). Furthermore, the survival
422 of anhydrous silicate crystal clusters, unfilled cracks and vesicles and the existence of significant
423 geochemical variation across each particle also support the idea of incomplete weathering, which is
424 in contrast to the intensely weathered coarse-grained micrometeorites shown in van Ginneken et al.,
425 (2016, Figs. 4C and 4D) that have no identifiable relict textures, extremely thick (>100µm) jarosite
426 overgrowth rims, densely layered limonite masses and homogenous back-scatter potential Z-values
427 throughout their cross-sections.

428 **5.2. Identifying atmospheric entry heating overprints** – The formation of dehydration cracks,
429 vesicular matrix, large rounded vesicles, interconnected channels, localized partial melting at the
430 micrometeorite's margin and simultaneous solid-state crystallization of the particle's internal
431 phyllosilicate matrix into (metamorphic) olivine are characteristic features and well-documented
432 effects of atmospheric entry heating (Suttle et al., 2017a; 2018). In the five micrometeorites studied
433 here; discontinuous magnetite rims and variable thickness igneous rims are, while the internal
434 textures contain either abundant dehydration cracks or vesicular matrix, this requires that their pre-
435 atmospheric phyllosilicates have experienced dehydration and dehydroxylation; releasing their water
436 content and developing significant porosity. Despite this process, much of their parent body textures
437 and relict anhydrous phases are preserved. This requires that partial melting was limited, suggesting
438 that peak temperatures did not exceed 1350°C, the solidus for chondritic matrix (Toppani et al., 2001)
439 and were likely <800°C (Suttle et al., 2017a; 2018). Further analysis of the atmospheric entry alteration
440 in these particles can be found in Suttle et al., (2018).

441 **5.3. Evidence for aqueous alteration** – Prior to their terrestrial alteration (by both atmospheric entry
442 [Section 5.2] and Antarctic weathering [Section 5.1]) these five micrometeorites were composed of
443 intermixed Fe and Mg-bearing phyllosilicate, whose relict textures reveal complex clusters of coarse
444 Fe-rich and finer-grained Mg-rich zones that overlap and cross-cut each other. Small (<5µm)
445 anhydrous silicate crystals are still present in all the micrometeorites studied, while larger crystals
446 (>10µm) are entirely absent from TAM19B-7 and rare in TAM15-11. These residual silicates have
447 anhedral morphologies and are typically fractured into a series of smaller grains with smooth, rounded
448 edges. They also commonly have thick phyllosilicate overgrowths, which may be layered (as in
449 TAM19B-18) or homogenous (as in TAM66-1). These textures are definitive evidence of significant
450 parent body aqueous alteration.

451 **5.3.1. Chondrule pseudomorphs and ghost CAIs** – Several rounded inclusions with elliptical or circular
452 shapes were found in TAM19B-7 (Fig.1A-D, 1H) and TAM66-1 (Fig.5A-F). These inclusions range in size
453 from approximately 100-300µm diameter, are composed primarily of amorphous dehydroxylated
454 phyllosilicate and Fe-oxides and mantled by compact, low porosity, fine-grained rims. In TAM66-1, the
455 two inclusions are composed of darker matrix with a Si-rich composition (Table.2, entries 36 & 37).
456 They contain many small relict anhydrous silicates (Table.2, entries 38-40) as well as rare Mg-Al spinels

457 (Table.2, entries 41 & 42). Meanwhile, the outer fine-grained rims have variable thicknesses and are
458 characterised by a vesicular texture and Fe-enriched composition (Table.2, entries 33-35). Conversely,
459 the inclusion cores in TAM19B-7 contain many rounded voids set within a fine-grained porous
460 groundmass, which is geochemically indistinguishable from the host micrometeorite's matrix. Thus,
461 the size, shape and presence of fine-grained rims in these inclusions are reminiscent of chondrules,
462 while their mineralogy (and in TAM19B-7 internal texture) are distinct from the igneous assemblages
463 of anhydrous silicates, FeNi metal, silicate glass and sulfides that are found in chondrules (Jones,
464 2012).

465 We interpret these inclusions as aqueously altered and subsequently flash heated chondrules. Initially,
466 their anhydrous igneous assemblages were replaced by Mg-rich phyllosilicates during aqueous
467 alteration, forming pseudomorphic chondrules. However, relict fragments of olivine and pyroxene
468 found in TAM66-1 (Fig.5C and 5D) survived alteration and attest to their polymineralic anhydrous
469 precursors. In contrast, in TAM19B-7 aqueous alteration is more advanced, resulting in the
470 geochemical homogenisation of the pseudomorphic chondrule with the surrounding matrix. Later,
471 during atmospheric entry, the altered chondrules experienced dehydration, dehydroxylation and
472 volatile de-gassing, resulting in the formation of dehydration cracks, the many large rounded vesicles
473 that dominate one of the inclusions in TAM19B-7 and the vesicular textures observed in the Fe-rich
474 fine-grained rims. However, because atmospheric entry heating was modest, partial melting was
475 limited and the parent body chondrule outlines and their fine-grained rims are, therefore, preserved.
476 Modified chondrules with high porosities, amorphous mineralogies and residual phyllosilicate are
477 relatively common, being found in abundance among the aqueously altered and thermally
478 metamorphosed class of CM chondrites (Nakamura, 2005; Lee et al., 2016), which are increasingly
479 considered to be an important and abundance group of parent bodies among the asteroid belt (Beck
480 et al., 2018).

481 Similar coarse-grained components are present in TAM19B-17; three large (~100µm diameter)
482 irregular shaped inclusions were identified in Figs. 2A and 2C. These inclusions are interpreted as
483 aqueously altered refractory phases. This is because they contain elevated abundances of refractory
484 elements, including Ca (0.3-7.9wt%), Al (1.8-5.1wt%) and Ti (0.1-0.2wt%), which are collected into
485 small bright spots, most likely representing residual mineral grains that survived alteration. The largest
486 refractory inclusion, shown in Fig.2D, is zoned irregular-shaped, with a porous core and radiating Fe-
487 rich rim. Chemical analysis of the inclusion's core (Table.2, entry 10) reveal a refractory silicate
488 composition approaching pyroxene (approximately $[\text{Mg,Fe,Ca}][\text{Al,Si}]\text{O}_3$), while the outer rim is dense,
489 Fe-enriched (Fig.2B) and of variable thickness. Although the inclusion core retains refractory material,
490 the margin has been entirely replaced with secondary minerals (assumed to be Fe-phyllosilicate),
491 which grew outwards from the host inclusion. These alteration products are, therefore, analogous to
492 the altered CAIs described from the C2 Tagish Lake meteorite by Takayama and Tomeoka (2012,
493 Fig.10). They observe large (~300µm diameter) zoned refractory assemblages, mantled by thick Fe-
494 rich phyllosilicate rims and whose dark cores have higher porosities, as well as residual refractory
495 minerals (perovskite and Al-spinel). The biggest difference between these two assemblages is the
496 presence of abundant carbonate in the Tagish Lake CAIs, which are not present in the
497 micrometeorite's inclusion. This is because the Tagish Lake lithology is carbonate-dominated while
498 micrometeorites have considerably less carbonate which is subsequently lost during atmospheric
499 entry heating, even at modest peak temperatures (<600°C, Nozaki et al., 2006). However, their
500 removal by thermal decomposition, along with the dehydration of phyllosilicate explains the presence

501 of rounded voids within the Fe-rich rim surrounding this inclusion (Fig.2D). Thus, the Ca-Al-Ti hotspots
502 within TAM19B-17 are interpreted as ghost CAIs and altered olivine clusters formed by advanced
503 aqueous alteration.

504 **5.3.2. Aqueous alteration in *matrix-only* micrometeorites** – The remaining two micrometeorites
505 (TAM19B-18 and TAM15-11) entirely lack coarse-grained components and instead are composed of
506 fine-grained matrix and isolated anhydrous silicates only. Variations in the back-scatter potential of
507 their matrix, coupled with their complex intergrown texture, imply multiple generations of secondary
508 mineral growth during aqueous alteration (Tomeoka et al., 1985; Veibel et al., 2012). In TAM15-11
509 several anhydrous silicate crystals have fractured morphologies, potentially indicating a fluid-assisted
510 brecciation phase or simultaneous impact brecciation and aqueous alteration – as suggested by
511 Zolensky et al., (1997), Rubin (2012), Hanna et al., (2015) and others. Conversely, in TAM19B-18,
512 anhydrous silicates are rounded and have thick phyllosilicate rims. Here, serpentine veins cross cut
513 these phyllosilicate rims (Fig.3B) and penetrate the silicate crystal's core. A stratigraphic relationship
514 can, therefore, be established: the phyllosilicate overgrowths must predate the serpentine veining.
515 This requires that aqueous alteration progressed initially by the growth of hydrated phyllosilicate
516 mantles that grew around the anhydrous silicates, initially using these crystals as a substrate and
517 replacing the original matrix, which was probably a porous mixture of amorphous Fe-rich silicate
518 (Noguchi et al., 2017). Furthermore, because the phyllosilicate rims in TAM19B-18 are layered, this
519 implies successive periods of growth, to develop a concentric layered texture. However, during a later
520 alteration period serpentine veins then grew through the rim and began to consume the olivine host
521 substrate. Similar chronologies, where anhydrous silicates are initially used as a substrate and later as
522 source material for secondary phyllosilicate growth, are characteristic alteration mechanisms of
523 hydrated chondrites and were previously described in Greenwood et al., (1994) and Takayama
524 Tomeoka (2012) within Cold Bokkeveld and Tagish Lake.

525 **5.4. Evaluating the extent of aqueous alteration in fine-grained micrometeorites** – We attempt to
526 quantify the degree of alteration affecting these giant TAM micrometeorites using two independent
527 evaluation methods (matrix geochemistry and modal mineralogy). Both approaches support the
528 hypothesis that these micrometeorites are intensely altered and derived from low petrologic subtype
529 parent bodies.

530 **5.4.1. Geochemical data** – The analysis of bulk matrix geochemistry in carbonaceous chondrites is one
531 method used for evaluating the degree of aqueous alteration. As alteration progresses, the
532 composition of the alteration fluid evolves. Increasing Mg concentrations occur due to the dissolution
533 of anhydrous silicate crystals, which are then re-precipitated as Mg-rich phyllosilicate (Velbel et al.,
534 2012; Elmaleh et al., 2015). Thus, bulk matrix “FeO/SiO₂” ratios decrease (Rubin et al., 2007), while
535 the Mg# increase (McSween 1979; 1987) as alteration advances. Therefore, the average bulk matrix
536 composition of a sample can be used to approximate the degree of alteration.

537 In Fig.9 we plot both major element geochemical ratios, obtained from a variety of hydrated chondritic
538 samples. This includes: 77 small (<100µm) Antarctic fine-grained micrometeorites, derived from the
539 Cap Prud'homme micrometeorite collection, as well as a selection of hydrated carbonaceous
540 chondrites (CI Ivuna and several CM2 chondrites), loaned from the NHM, London. The majority of
541 these samples were previously analysed in Suttle et al., (2017a) and their geochemical data are
542 included here as a supplementary file (Fig.S1). In addition, we plot the bulk matrix data from our five
543 giant TAM micrometeorites. A linear regression trendline is plotted through the Cap Prud'homme

544 micrometeorites. This logarithmic [$Mg\# = -25.81 \ln(FeO/SiO_2) + 48.19$] line-of-best-fit
545 demonstrates a strong negative correlation ($R^2=0.86$) between the Fe and Mg concentrations within a
546 micrometeorite's matrix. This can, therefore, be viewed as a progressive aqueous alteration trend
547 along which hydrated chondritic materials lie. More altered samples plot in the top left quadrant, at
548 high Mg# values and low FeO/SiO₂ values.

549 TAM19B-18 lies close to the alteration trendline (with average values of FeO/SiO₂=1.46, Mg#=33.9)
550 while the remaining four micrometeorites have anomalously low Mg concentrations and, therefore,
551 plot in the lower left quadrant of Fig.9. Their low-Mg values are inconsistent with a hydrated chondritic
552 sample and, instead, suggest that a later geochemical process has subsequently altered their matrix
553 composition. In section 5.1 we noted that the TAM micrometeorites studied here are affected by
554 terrestrial weathering. As a result, the bulk matrix compositions, shown in Figs.6 & 7, demonstrate
555 depletions in Mg due to leaching and mobilisation by terrestrial fluids (Kurat et al., 1994; van Ginneken
556 et al., 2016). However, an attempt can be made to correct for the missing Mg in these micrometeorites
557 by using the alteration trendline, defined from the small Cap Prud'homme micrometeorites as a guide
558 and raising the Mg# values of the intensely weathered micrometeorites until each data point plots
559 directly on the aqueous alteration trendline. This provides an approximation of their pre-terrestrial
560 Mg concentration and allows us to estimate their degree of alteration.

561 Assuming these corrected Mg# values are approximately correct; the five micrometeorites appear to
562 span a range of alteration degrees; their relative sequence from least to most altered is: TAM19B-
563 18<TAM19B-17<TAM66-1<TAM19B-7<TAM15-11. Furthermore, assuming distance along the
564 alteration trendline is proportional to the degree of alteration, then TAM19B-18 appears to be
565 significantly less-altered than the remaining four micrometeorites. Using the hydrated carbonaceous
566 chondrites as a reference, the four most altered micrometeorites plot in a tight group and with similar
567 positions to that of ALHA 81002, Mighei and Cold Bokkeveld. These meteorites are characterised by
568 moderate to intense aqueous alteration histories and accordingly have been assigned low petrologic
569 subtypes in several studies (Greenwood et al., 1994; Zolensky et al., 1997), including that of Howard
570 et al., (2015) who classified all three meteorites with a petrologic subtype of 1.4.

571 In contrast, TAM19B-18 plots further down the alteration trendline and close to Jbilet Winselwan. This
572 meteorite was previously investigated in Friend et al., (2018), who concluded that Jbilet Winselwan is
573 only mildly altered, with a petrologic subtype between CM2.5-2.6 (on the scale of Rubin et al., [2007]).
574 However, since this chondrite is a breccia, composed of many diverse clasts, other studies have arrived
575 at distinctly different conclusions, as in the case of Pernet-Fisher et al., (2014) who classified Jiblet
576 Winselwan as a CM2.0-2.3 petrologic subtype (also on the scale of Rubin et al., [2007]). Our sample of
577 Jbilet Winselwan (P18927) has a relatively Fe-rich matrix (Mg# 39) and appears less altered than the
578 other CM2 chondrites analysed here, suggesting a moderate degree of alteration.

579 **5.4.2. Phyllosilicate fraction** – Another method used to evaluate the degree of aqueous alteration in
580 chondrites is modal mineralogy, developed by Bland et al., (2004) and Howard et al., (2009; 2015) and
581 later employed for CI chondrites by King et al., (2015). This approach calculates the phyllosilicate
582 fraction in a hydrated chondrite as a proxy for the degree of secondary mineral replacement. We
583 calculated the approximate phyllosilicate fraction in the five TAM micrometeorites using their exposed
584 cross-sections to determine major mineral abundances. For each particle their high-resolution BSE
585 images and EDX maps were used to identify the abundance of phyllosilicate and anhydrous silicate as
586 a percentage of the particle's total surface area (their calculated phyllosilicate fractions are shown in

587 Table.1). Using the single element Mg-K α EDX maps, anhydrous silicate crystals are easily identified as
588 bright, dense objects with clear boundaries.

589 All five TAM micrometeorites have high phyllosilicate fractions, ranging between 93-98% (TAM15-11:
590 98%, TAM19B-7: 97%, TAM19B-17: 96%, TAM66-1: 95% and TAM19B-18: 93%). These are plotted in
591 Fig.10, against the existing data, calculated by Howard et al., (2015), from CM, CR and ungrouped C2
592 chondrites. Using this modal mineralogy metric, the inferred subtypes are at the extreme end-
593 member of the range with petrologic subtypes <1.1. They therefore represent samples from nearly
594 completely hydrated chondrites, closely associated with the C1 class. In addition to intense alteration
595 degrees, the relative alteration sequence of the five samples is similar to the relative sequence
596 determined from the geochemical data; from least to most altered this is: TAM19B-18<TAM66-
597 1<TAM19B-17 <TAM19B-7<TAM15-11.

598 However, because this study analyses such small particles, these micrometeorites are unlikely to be
599 representative samples of their parent bodies. Consequently, their source asteroid's petrologic
600 subtype is likely to be less-altered than these data suggest. This is because, further analysis of a larger
601 cm-scale fragments is likely to uncover additional coarse-grained anhydrous components. We
602 therefore, suggest that the assigned petrologic subtypes should be viewed as the maximum possible
603 degree of alteration.

604 **5.5. Shock deformation in fine-grained micrometeorites** – An increasingly common observation
605 among CM chondrites is the association of higher degrees of aqueous alteration and the presence of
606 impact deformation features, including brecciation and pervasive petrofabrics (Zolensky et al., 1997;
607 Rubin, 2012; Hanna et al., 2015; Lindgren et al., 2015). Foliation within chondrites is discernible
608 through the alignment of phyllosilicates (Rubin et al., 2007; Rubin, 2012), which wrap around
609 chondrules (Hanna et al., 2015), while the presence of subparallel fractures, mineralised veins
610 (Lindgren et al., 2015), cataclasis textures (Hanna et al., 2015) and aligned elongated, elliptical or
611 crushed chondrules (Lindgren et al., 2015) also attest to impact processing. The apparent correlation
612 between pervasive shock fabrics and enhanced aqueous alteration has, therefore, led to the
613 suggestion that impact events provide the necessary heat energy to drives hydrothermal alteration
614 on primitive asteroids (Rubin, 2012; Lindgren et al., 2015).

615 In contrast, shock deformation in micrometeorites was initially reported by Genge, (2007) and inferred
616 from the presence of shock blackening, metal-sulfide melt veins, similar to those identified in shocked
617 chondrules within olivine grains with numerous subdomains, similar to mosaic extinction patterns that
618 develop at high shock pressures (20-60GPa, Scott et al., 1992) and from the presence of highly
619 vesicular glass, representing shock melting at extreme peak pressures >50GPa (Tomeoka et al., 1999).
620 More recently, low-grade (<5GPa), subtle shock fabrics in small fine-grained Antarctic
621 micrometeorites were revealed through the alignment of dehydration cracks, vesicles and fractures.
622 A preferred orientation was identified in the majority of micrometeorites analysed (80%, Suttle et al.,
623 2017c). These petrofabrics form when aligned phyllosilicates within the matrix of hydrated dust grains
624 are subject to atmospheric entry heating, forming dehydration cracks, and later vesicles. The
625 formation of voids is partially constrained by the orientation of the host phyllosilicates (Nozaki et al.,
626 2006; Suttle et al., 2017c) and, therefore, provides a metric to trace pre-atmospheric anisotropies
627 within the micrometeorite that were present on the parent asteroid (Suttle et al., 2017c).

628 Our study further supports the link between shock features and aqueous alteration in hydrated
629 carbonaceous chondrites. This is because four of the five micrometeorites studied here are both
630 intensely altered and show evidence of a distinct petrofabric with a uniaxial or pseudo-uniaxial
631 distribution (Fig.11). They share low entropy values, lower than or equivalent to the entropy values
632 obtained from Cold Bokkeveld ($S=2.619$) and Jbilet Winselwan ($S=2.783$), which are recognised as
633 regolith breccias with documented shock textures (Metzler et al., 1992; Zolensky et al., 2016).
634 Furthermore, in the case of TAM19B-7 the elongation direction of the elliptical chondrule
635 pseudomorph is also parallel to the elongation direction of the particle's voids strongly suggesting an
636 impact origin to this micrometeorite's petrofabric. However, we do not find a close correlation
637 between each micrometeorite's petrofabric strength (entropy value, S) and their relative degree of
638 aqueous alteration, as determined by either the modal mineralogy or matrix geochemistry metrics.
639 Thus, these two geological processes are not directly related.

640 **6. Implications**

641 **6.1. Aqueous alteration among the fine-grained micrometeorite flux** – The apparent paucity of
642 recognisable, whole chondrules among Antarctic micrometeorite collections, <<1% among the SPWW
643 collection (Taylor et al., 2012) and <3% within the Larkman Nunatak collection (Genge et al., 2018,
644 Fig.12) has previously been taken as evidence that fine-grained micrometeorites sample a chondrule-
645 poor, matrix-rich parent body, related to, but distinct from, the established hydrated chondrite groups
646 (Engrand and Maurette, 1998; Varela and Kurat, 2009 (and references therein); Reshma et al., 2013).
647 However, the small size (<100 μm) of most Antarctic micrometeorites prevents individual grains from
648 sampling whole chondrules (Fig.12 in Genge, 2006), whose diameters typically exceed 250 μm (Jones,
649 2012). Instead, chondrules are represented among micrometeorite collections as fragmented shards
650 and classified as coarse-grained or composite particles (Genge, et al., 2005; 2008; van Ginneken et al.,
651 2017).

652 Estimates for the abundance of coarse and composite micrometeorites are, at present, poorly
653 constrained but likely represent between 10-30% of the total micrometeorite flux (Kurat et al., 1994;
654 Taylor et al., 2012). However, up to 70% of this material is geochemically related to ordinary chondrite
655 precursors (Genge, 2008), leaving little remaining material to account for the hydrated chondrule
656 budget (perhaps as little as 2% of the total flux). For comparison, most CM and CR chondrites are
657 composed of ~20-50% chondrules by volume (Weisberg, et al., 2006). Thus, it appears that hydrated
658 fine-grained micrometeorites – like those analysed in this study – are moderately-to-severely
659 underrepresented in C2 chondrule material, by potentially up to 1 order of magnitude.

660 Among the TAM micrometeorite collection, the analysis of significantly larger and, therefore, more
661 representative micrometeorites should result in the identification of CM, CR and C2 ungrouped
662 micrometeorites containing intact chondrules. However, only a single micrometeorite with an
663 unaltered anhydrous CM chondrule (TAM2.1i, Fig.5 in van Ginneken et al., 2012) has so far been
664 identified among a population of >100 TAM micrometeorites. Thus, unaltered and unfragmented
665 chondrules derived from hydrated chondritic parent bodies are extremely rare.

666 In this study, we investigated five giant fine-grained micrometeorites, representing >2mm² of fine-
667 grained matrix. Despite this relatively large area, only 4-5 pseudomorphic chondrules and several
668 small altered CAIs were identified, giving a combined chondrule-to-matrix ratio of just 6.45%
669 ([0.14/2.22]mm²). We therefore argue that these micrometeorites represent samples of intensely

670 aqueously altered chondritic matrix, with genetic affinities to the C1 chondrites. Likewise, it seems
671 probable that a significant fraction of micrometeorite flux reaching the Earth today, must also
672 originate from equivalent intensely aqueously altered asteroids. This scenario would then explain a
673 reduced flux of recognisable chondrule material from hydrated carbonaceous parent bodies whilst
674 also supporting the well-documented genetic match between (most) fine-grained micrometeorites
675 and fine-grained CM/CR/C2 matrix.

676 **6.2. The parent bodies of fine-grained micrometeorites** – Owing to the unique P-R drag delivery
677 mechanism, cosmic dust rapidly spirals into the inner solar system (Klačka et al., 2014). Consequently,
678 micrometeorites are expected to sample significantly more parent bodies than meteorites and, thus,
679 sample a more diverse population of asteroids. This will necessarily include contributions from both
680 the established carbonaceous chondrite groups as well as otherwise unsampled chondritic parent
681 bodies. We should, therefore, expect micrometeorite collections to contain both particles with direct
682 affinities to CM, CR and CI chondrites as well as micrometeorites whose petrographic affinities are
683 inconsistent with established groups.

684 However, we also propose that some of the observed petrographic differences between fine-grained
685 micrometeorites and CM/CR/CI chondrites are explainable as a result of sampling biases. Because the
686 petrographic properties of established carbonaceous chondrite groups are defined only from
687 meteorites, and since meteorites are known to originate from a limited number of parent bodies
688 (~110, Greenwood et al., 2016), it is probable that the full range of petrographic properties for each
689 chondrite group (CR, CM, CI etc.) are not accurately sampled. Likewise, it is also possible that many of
690 the fine-grained micrometeorites originate from the same parent bodies as meteorites but are not
691 recognised as such because they have geochemical, organic matter or isotopic signatures which fall
692 outside the defined range. Thus, we suggest that some of the differences between fine-grained
693 micrometeorites and CM/CR/CI chondrites are a product of sampling issues.

694 **7. Conclusions**

695 This study investigated five giant fine-grained micrometeorites whose petrographies are dominated
696 by hydrated secondary minerals formed during advanced aqueous alteration. They contain multiple
697 generations of phyllosilicate growth, evidenced by cross-cutting relationships, variable cation
698 compositions and a range of grain sizes. Meanwhile, unaltered coarse-grained, structural components
699 such as chondrules, CAIs and AOAs are either rare or entirely absent, having been replaced by
700 indistinct chondrule pseudomorphs and partially consumed CAIs. These micrometeorites, therefore,
701 share many similarities with the intensely altered CM1, CR1 and CI carbonaceous chondrites. Four of
702 the five micrometeorites also show evidence of pervasive uniaxial petrofabrics, most likely generated
703 by impact processing. This is most evident in TAM19B-7, in which the alignment of matrix
704 phyllosilicates is parallel to the elongation direction of a compacted chondrule pseudomorph.

705 On the basis of our findings and previous studies researching small fine-grained micrometeorites we
706 propose that much of the fine-grained dust flux is most likely derived from established hydrated
707 carbonaceous chondrites groups and that their intensely altered compositions suggest the C-type
708 asteroid population contains many hydrated bodies with high water contents.

709 **8. Acknowledgements**

710 The data presented in this paper were acquired during my PhD research at Imperial College London and the
711 NHM and funded by the Science and Technology Council (STFC) (ST/M503526/1). Research continued whilst I
712 attended a post-doc research position at the University of Pisa, which is funded through 2 Italian research grants
713 MIUR: PNRA16_00029 [Programma Nazionale delle Ricerche in Antartide – CUP I52F17001050005] and
714 PRIN2015_20158W4JZ7 [CUP I52F15000310001 for the "Meteoriti Antartiche"]. L. Folco is also supported
715 through the same research grants, while M. Genge and S. Russell are funded by the STFC grants (ST/J001260/1
716 and ST/M00094X/1 respectively). We thank J. Spratt, T. Góral and T. Salge at the NHM, London for their support
717 and advice during and analytical acquisition. Further, we thank 2 anonymous reviewers and Kieran Howard for
718 their suggestions and comments during the review process as well as associate editor Eric Quirico and Executive
719 editor Marc Norman for their handling of this manuscript and advice.

720 9. References

- 721 Alexander, C.M.D., Taylor, S., Delaney, J.S., Ma, P. and Herzog, G.F., 2002. Mass-dependent fractionation of Mg,
722 Si, and Fe isotopes in five stony cosmic spherules. *Geochim. Cosmochim. Acta* **66**, 173-183, doi:10.1016/S0016-
723 7037(01)00764-5.
- 724 Battandier, M., Bonal, L., Quirico, E., Beck, P., Engrand, C., Duprat, J. and Dartois, E., 2018. Characterization of
725 the organic matter and hydration state of Antarctic micrometeorites: A reservoir distinct from carbonaceous
726 chondrites. *Icarus* **306**, 74-93, doi:10.1016/j.icarus.2018.02.002.
- 727 Beck, P., Maturilli, A., Garenne, A., Vernazza, P., Helbert, J., Quirico, E. and Schmitt, B., 2018. What is controlling
728 the reflectance spectra (0.35–150 µm) of hydrated (and dehydrated) carbonaceous chondrites?. *Icarus* **313**, 124-
729 138, doi:10.1016/j.icarus.2018.05.010.
- 730 Bland, P.A., Kelley, S.P., Berry, F.J., Cadogan, J.M. and Pillinger, C.T., 1997. Artificial weathering of the ordinary
731 chondrite Allegan: Implications for the presence of Cl—as a structural component in akaganeite. *American*
732 *Mineralogist* **82**, 1187-1197, doi:10.2138/am-1997-11-1215.
- 733 Bland, P.A., Cressey, G. and Menzies, O.N., 2004. Modal mineralogy of carbonaceous chondrites by X-ray
734 diffraction and Mössbauer spectroscopy. *Meteoritics Planet.Sci.* **39**, 3-16, doi:10.1111/j.1945-
735 5100.2004.tb00046.x.
- 736 Bland, P.A., Jackson, M.D., Coker, R.F., Cohen, B.A., Webber, J.B.W., Lee, M.R., Duffy, C.M., Chater, R.J., Ardakani,
737 M.G., McPhail, D.S. and McComb, D.W., 2009. Why aqueous alteration in asteroids was isochemical: High
738 porosity≠ high permeability. *Earth Planet. Sci. Lett.*, **287**, 559-568, doi:10.1016/j.epsl.2009.09.004.
- 739 Browning, L.B., McSween Jr, H.Y. and Zolensky, M.E., 1996. Correlated alteration effects in CM carbonaceous
740 chondrites. *Geochim. Cosmochim. Acta* **60**, 2621-2633, doi:10.1016/0016-7037(96)00121-4.
- 741 Ciesla, F.J., Lauretta, D.S., Cohen, B.A. and Hood, L.L., 2003. A nebular origin for chondritic fine-grained
742 phyllosilicates. *Science*, **299**, 549-552, doi:10.1126/science.1079427.
- 743 Doyle, P.M., Jogo, K., Nagashima, K., Krot, A.N., Wakita, S., Ciesla, F.J. and Hutcheon, I.D., 2015. Early aqueous
744 activity on the ordinary and carbonaceous chondrite parent bodies recorded by fayalite. *Nature*
745 *communications*, **6**, 7444, doi:10.1038/ncomms8444.
- 746 Elmaleh, A., Bourdelle, F., Caste, F., Benzerara, K., Leroux, H. and Devouard, B., 2015. Formation and
747 transformations of Fe-rich serpentines by asteroidal aqueous alteration processes: A nanoscale study of the
748 Murray chondrite. *Geochim. Cosmochim. Acta* **158**, 162-178, doi:10.1016/j.gca.2015.03.007.
- 749 Engrand, C. and Maurette, M., 1998. Carbonaceous micrometeorites from Antarctica. *Meteoritics Planet.Sci.* **33**,
750 565-580, doi:10.1111/j.1945-5100.1998.tb01665.x.
- 751 Folco, L., Rochette, P., Perchiazzi, N., d'Orazio, M., Laurenzi, M.A. and Tiepolo, M., 2008. Microtektites from
752 Victoria Land Transantarctic Mountains. *Geology*, **36**, 291-294, doi:10.1130/G24528A.

753 Friend, P., Hezel, D.C., Barrat, J.A., Zipfel, J., Palme, H. and Metzler, K., 2018. Composition, petrology, and
754 chondrule-matrix complementarity of the recently discovered Jbilet Winselwan CM2 chondrite. *Meteoritics*
755 *Planet.Sci*, doi:10.1111/maps.13139.

756 Genge, M.J., 2002. Hydrated Chondrule Fragments Amongst Micrometeorites. 65th Annual Meeting of the
757 *Meteoritical Society*, held July 21-26, 2002 in Los Angeles, California. (abstract #5102).

758 Genge, M.J., 2006. Igneous rims on micrometeorites. *Geochim. Cosmochim. Acta* **70**, 2603-2621,
759 doi:10.1016/j.gca.2006.02.005.

760 Genge, M.J., 2007. Evidence for Shock in Micrometeorites: 70th Annual Meeting of the *Meteoritical Society*, held
761 August 13-17, Tucson, Arizona. (abstract #5007).

762 Genge, M.J., 2008. Koronis asteroid dust within Antarctic ice. *Geology* **36**, 687-690, doi:10.1130/G24493A.1.

763 Genge, M.J., Gileski, A. and Grady, M.M., 2005. Chondrules in Antarctic micrometeorites *Meteoritics Planet.Sci.*
764 **40**, 225-238, doi:10.1111/j.1945-5100.2005.tb00377.x.

765 Genge, M.J., Engrand, C., Gounelle, M. and Taylor, S., 2008. The classification of micrometeorites. *Meteoritics*
766 *Planet.Sci.* **43**, 497-515, doi:10.1111/j.1945-5100.2008.tb00668.x.

767 Genge, M.J., van Ginneken, M., Suttle, M.D. and Harvey, R.P., 2018. Accumulation mechanisms of
768 micrometeorites in an ancient supraglacial moraine at Larkman Nunatak, Antarctica. *Meteoritics Planet.Sci.*
769 doi:10.1111/maps.13107

770 Greenwood, R.C., Lee, M.R., Hutchison, R. and Barber, D.J., 1994. Formation and alteration of CAIs in Cold
771 Bokkeveld (CM2). *Geochim. Cosmochim. Acta* **58**, 1913-1935, doi:10.1016/0016-7037(94)90424-3.

772 Greenwood, R.C., Burbine, T.H., Miller, M.F. and Franchi, I.A., 2017. Melting and differentiation of early-formed
773 asteroids: The perspective from high precision oxygen isotope studies. *Chemie der Erde* **77**, 1-43,
774 doi:10.1016/j.chemer.2016.09.005.

775 Hanna, R.D., Ketcham, R.A., Zolensky, M. and Behr, W.M., 2015. Impact-induced brittle deformation, porosity
776 loss, and aqueous alteration in the Murchison CM chondrite. *Geochim. Cosmochim. Acta* **171**, 256-282,
777 doi:10.1016/j.gca.2015.09.005.

778 Harju, E.R., Rubin, A.E., Ahn, I., Choi, B.G., Ziegler, K. and Wasson, J.T., 2014. Progressive aqueous alteration of
779 CR carbonaceous chondrites. *Geochim. Cosmochim. Acta* **58**, 267-292, doi:10.1016/j.gca.2014.04.048.

780 Hewins, R.H., Bourot-Denise, M., Zanda, B., Leroux, H., Barrat, J.A., Humayun, M., Göpel, C., Greenwood, R.C.,
781 Franchi, I.A., Pont, S. and Lorand, J.P., 2014. The Paris meteorite, the least altered CM chondrite so far. *Geochim.*
782 *Cosmochim. Acta* **124**, 190-222, doi:10.1016/j.gca.2013.09.014.

783 Hezel, D.C., Russell, S.S., Ross, A.J. and Kearsley, A.T., 2008. Modal abundances of CAIs: Implications for bulk
784 chondrite element abundances and fractionations. *Meteoritics Planet.Sci.* **43**, 1879-1894, doi:10.1111/j.1945-
785 5100.2008.tb00649.x.

786 Howard, K.T., Benedix, G.K., Bland, P.A. and Cressey, G., 2009. Modal mineralogy of CM2 chondrites by X-ray
787 diffraction (PSD-XRD). Part 1: Total phyllosilicate abundance and the degree of aqueous alteration. *Geochim.*
788 *Cosmochim. Acta* **73**, 4576-4589, doi:10.1016/j.gca.2009.04.038.

789 Howard, K.T., Alexander, C.O.D., Schrader, D.L. and Dyl, K.A., 2015. Classification of hydrous meteorites (CR, CM
790 and C2 ungrouped) by phyllosilicate fraction: PSD-XRD modal mineralogy and planetesimal environments.
791 *Geochim. Cosmochim. Acta* **149**, 206-222, doi:10.1016/j.gca.2014.10.025

792 Jones, R.H., 2012. Petrographic constraints on the diversity of chondrule reservoirs in the protoplanetary disk.
793 *Meteoritics Planet.Sci.* **47**, 1176-1190, doi:10.1111/j.1945-5100.2011.01327.x.

794 King, A.J., Schofield, P.F., Howard, K.T. and Russell, S.S., 2015. Modal mineralogy of CI and CI-like chondrites by
795 X-ray diffraction. *Geochim. Cosmochim. Acta* **165**, 148-160, doi:10.1016/j.gca.2015.05.038.

796 King, A.J., Schofield, P.F. and Russell, S.S., 2017. Type 1 aqueous alteration in CM carbonaceous chondrites:
797 Implications for the evolution of water-rich asteroids. *Meteoritics Planet. Sci.* **52**, 1197-1215,
798 doi:10.1111/maps.12872

799 Klačka, J., Petržala, J., Pástor, P. and Kómar, L., 2014. The Poynting–Robertson effect: A critical perspective. *Icarus*
800 **232**, 249-262, doi:10.1016/j.icarus.2012.06.044.

801 Krot, A.N., Petaev, M.I. and Yurimoto, H., 2004. Amoeboid olivine aggregates with low-Ca pyroxenes: a genetic
802 link between refractory inclusions and chondrules?. *Geochim. Cosmochim. Acta* **68**, 1923-1941,
803 doi:10.1016/j.gca.2003.10.026.

804 Kurat, G., Brandstaetter, F., Maurette, M. and Coeberl, C., 1991. Cl-like micrometeorites from Cap Prudhomme,
805 Antarctica. *Lunar Planet. Sci. XXIII*. Lunar Planet. Inst., Houston. #747(abstr.)

806 Kurat, G., Koeberl, C., Presper, T., Brandstätter, F. and Maurette, M., 1994. Petrology and geochemistry of
807 Antarctic micrometeorites. *Geochim. Cosmochim. Acta* **58**, 3879-3904, doi:10.1016/0016-7037(94)90369-7.

808 Le Guillou, C., Changela, H.G. and Brearley, A.J., 2015. Widespread oxidized and hydrated amorphous silicates in
809 CR chondrites matrices: Implications for alteration conditions and H₂ degassing of asteroids. *Earth and Planet.*
810 *Sci. Lett.*, **420**, 162-173, doi:10.1016/j.epsl.2015.02.031.

811 Lee, M.R., Lindgren, P., Sofe, M.R., Alexander, C.O.D. and Wang, J., 2012. Extended chronologies of aqueous
812 alteration in the CM2 carbonaceous chondrites: Evidence from carbonates in Queen Alexandra Range
813 93005. *Geochim. Cosmochim. Acta* **92**, 148-169, doi:10.1016/j.gca.2012.06.005.

814 Lee, M.R., Sofe, M.R., Lindgren, P., Starkey, N.A. and Franchi, I.A., 2013. The oxygen isotope evolution of parent
815 body aqueous solutions as recorded by multiple carbonate generations in the Lonewolf Nunataks 94101 CM2
816 carbonaceous chondrite. *Geochim. Cosmochim. Acta* **121**, 452-466, doi:10.1016/j.gca.2013.07.010.

817 Lee, M.R., Lindgren, P. and Sofe, M.R., 2014. Aragonite, breunnerite, calcite and dolomite in the CM
818 carbonaceous chondrites: High fidelity recorders of progressive parent body aqueous alteration. *Geochim.*
819 *Cosmochim. Acta* **144**, 126-156, doi:10.1016/j.gca.2014.08.019.

820 Lee, M.R. and Lindgren, P., 2016. Aqueous alteration of chondrules from the Murchison CM carbonaceous
821 chondrite: Replacement, pore filling, and the genesis of polyhedral serpentine. *Meteoritics Planet. Sci.* **51**, 1003-
822 1021, doi:10.1111/maps.12644.

823 Leroux, H., Cuvillier, P., Zanda, B. and Hewins, R.H., 2015. GEMS-like material in the matrix of the Paris meteorite
824 and the early stages of alteration of CM chondrites. *Geochim. Cosmochim. Acta* **170**, 247-265,
825 doi:10.1016/j.gca.2015.09.019.

826 Lindgren, P., Hanna, R.D., Dobson, K.J., Tomkinson, T. and Lee, M.R., 2015. The paradox between low shock-
827 stage and evidence for compaction in CM carbonaceous chondrites explained by multiple low-intensity impacts.
828 *Geochim. Cosmochim. Acta* **148**, 159-178, doi: 10.1016/j.gca.2014.09.014.

829 Lodders, K., 2003. Solar system abundances and condensation temperatures of the elements. *The Astrophys.*
830 *Journal* **591**, 1220-1247, doi:10.1086/375492.

831 Maharaj, S.V. and Hewins, R.H., 1994. Clues to chondrule precursors: An investigation of vesicle formation in
832 experimental chondrules. *Geochim. Cosmochim. Acta* **58**, 1335-1342, doi:10.1016/0016-7037(94)90385-9.

833 Marrocchi, Y., Gounelle, M., Blanchard, I., Caste, F. and Kearsley, A.T., 2014. The Paris CM chondrite: Secondary
834 minerals and asteroidal processing. *Meteoritics Planet. Sci.* **49**, 1232-1249, doi:10.1111/maps.12329.

835 McSween Jr, H.Y., 1979. Alteration in CM carbonaceous chondrites inferred from modal and chemical variations
836 in matrix. *Geochim. Cosmochim. Acta* **43**, 1761-1770, doi:10.1016/0016-7037(79)90024-3.

837 McSween Jr, H.Y., 1987. Aqueous alteration in carbonaceous chondrites: Mass balance constraints on matrix
838 mineralogy. *Geochim. Cosmochim. Acta* **51**, 2469-2477, doi:10.1016/0016-7037(87)90298-5.

839 Metzler, K., Bischoff, A., and Stöffler, D. 1992. Accretionary dust mantles in CM chondrites: Evidence for solar
840 nebula processes. *Geochim. Cosmochim. Acta* **56**, 2873-2897, doi:10.1016/0016-7037(92)90365-P.

841 Nakamura, T., 2005. Post-hydration thermal metamorphism of carbonaceous chondrites. *Journ. Mineralog.*
842 *Petrolog. Sci.* **100**, 260-272, doi:10.2465/jmps.100.260.

843 Noguchi, T., Yabuta, H., Itoh, S., Sakamoto, N., Mitsunari, T., Okubo, A., Okazaki, R., Nakamura, T., Tachibana, S.,
844 Terada, K. and Ebihara, M., 2017. Variation of mineralogy and organic material during the early stages of aqueous
845 activity recorded in Antarctic micrometeorites. *Geochim. Cosmochim. Acta* **208**, 119-144,
846 doi:10.1016/j.gca.2017.03.034.

847 Nozaki, W., Nakamura, T. and Noguchi, T., 2006. Bulk mineralogical changes of hydrous micrometeorites during
848 heating in the upper atmosphere at temperatures below 1000C. *Meteoritics Planet. Sci.* **41**, 1095-1114,
849 doi:10.1111/j.1945-5100.2006.tb00507.x.

850 Pernet-Fisher, J.F., Howarth, G.H., Barry, P.H., Bodnar, R.J. and Taylor, L.A., 2014, March. The extent of aqueous
851 alteration within the Jbilet Winselwan CM2 chondrite. *Lunar Planet. Sci. XXXV Lunar Planet. Inst., Houston.*
852 *#2386(abstr.)*.

853 Pignatelli, I., Marrocchi, Y., Vacher, L.G., Delon, R. and Gounelle, M., 2016. Multiple precursors of secondary
854 mineralogical assemblages in CM chondrites. *Meteoritics Planet. Sci.* **51**, 785-805, doi:10.1111/maps.12625.

855 Reshma, K., Rudraswami, N.G. and Prasad, M.S., 2013. Chondrule-like object from the Indian Ocean cosmic
856 spherules. *Journ. Earth System Sci.* **122**, 1161-1171, doi:10.1007/s12040-013-0333-8.

857 Rietmeijer, F.J., 1991. Aqueous alteration in five chondritic porous interplanetary dust particles. *Earth Planet.*
858 *Sci. Lett.* **102**, 48-157, doi:10.1016/0012-821X(91)90004-2.

859 Rubin, A.E., 2012. Collisional facilitation of aqueous alteration of CM and CV carbonaceous chondrites. *Geochim.*
860 *Cosmochim. Acta* **90**, 181-194, doi:10.1016/j.gca.2012.05.016.

861 Rubin, A.E. and Wasson, J.T., 1986. Chondrules in the Murray CM2 meteorite and compositional differences
862 between CM-CO and ordinary chondrite chondrules. *Geochim. Cosmochim. Acta* **50**, 307-315, doi:10.1016/0016-
863 7037(86)90179-1.

864 Rubin, A.E., Trigo-Rodríguez, J.M., Huber, H. and Wasson, J.T., 2007. Progressive aqueous alteration of CM
865 carbonaceous chondrites. *Geochim. Cosmochim. Acta* **71**, 2361-2382, doi:10.1016/j.gca.2007.02.008.

866 Scott, E.R., Keil, K. and Stoeffler, D., 1992. Shock metamorphism of carbonaceous chondrites. *Geochim.*
867 *Cosmochim. Acta* **56**, 4281-4293, doi:10.1016/0016-7037(92)90268-N.

868 Steele, I.M., 1992. Olivine in Antarctic micrometeorites: Comparison with other extraterrestrial olivine. .
869 *Geochim. Cosmochim. Acta* **56**, 2923-2929, doi:10.1016/0016-7037(92)90368-S.

870 Suavet, C., Rochette, P., Kars, M., Gattacceca, J., Folco, L. and Harvey, R.P., 2009. Statistical properties of the
871 Transantarctic Mountains (TAM) micrometeorite collection. *Polar Sci.* **3**, 100-109,
872 doi:10.1016/j.polar.2009.06.003.

873 Suavet, C., Alexandre, A., Franchi, I.A., Gattacceca, J., Sonzogni, C., Greenwood, R.C., Folco, L. and Rochette, P.,
874 2010. Identification of the parent bodies of micrometeorites with high-precision oxygen isotope ratios. *Earth*
875 *Planet. Sci. Lett.* **293**, 313-320, doi:10.1016/j.epsl.2010.02.046.

876 Suavet, C., Gattacceca, J., Rochette, P. and Folco, L., 2011. Constraining the terrestrial age of micrometeorites
877 using their record of the Earth's magnetic field polarity. *Geology* **39**, 123-126, doi:10.1130/G31655.1.

878 Suttle, M.D., Genge, M.J., Folco, L. and Russell, S.S., 2017a. The thermal decomposition of fine-grained
879 micrometeorites, observations from mid-IR spectroscopy. *Geochim. Cosmochim. Acta* **206**, 112-136,
880 doi:10.1016/j.gca.2017.03.002.

881 Suttle, M.D. and Genge, M.J., 2017b. Diagenetically altered fossil micrometeorites suggest cosmic dust is
882 common the geological record. *Earth Planet. Sci. Lett.* **476**, 132-142, doi:10.1016/j.epsl.2017.07.052.

883 Suttle, M.D., Genge, M.J., Russell, S.S., 2017c. Shock fabrics in fine-grained micrometeorites. *Meteoritics Planet.*
884 *Sci.* doi:10.1111/maps.12927.

885 Suttle, M.D., Genge, M.J., Folco, L., Lin, Q., Russell, S.S., and Najorka, J. 2018. The atmospheric entry of fine-
886 grained micrometeorites: the role of volatile gases in heating and fragmentation. *Geochim. Cosmochim. Acta*,
887 *submitted*.

888 Takayama, A. and Tomeoka, K., 2012. Fine-grained rims surrounding chondrules in the Tagish Lake carbonaceous
889 chondrite: Verification of their formation through parent-body processes. *Geochim. Cosmochim. Acta* **98**, 1-18,
890 doi:10.1016/j.gca.2012.08.015.

891 Takir, D., Emery, J.P., Mcsween, H.Y., Hibbitts, C.A., Clark, R.N., Pearson, N. and Wang, A., 2013. Nature and
892 degree of aqueous alteration in CM and CI carbonaceous chondrites. *Meteoritics Planet. Sci.* **48**, 1618-1637,
893 doi:10.1111/maps.12171.

894 Taylor, S., Matrajt, G. and Guan, Y., 2012. Fine-grained precursors dominate the micrometeorite flux. *Meteoritics*
895 *Planet. Sci.* **47**, 550-564, doi:10.1111/j.1945-5100.2011.01292.

896 Tomeoka, K. and Buseck, P.R., 1985. Indicators of aqueous alteration in CM carbonaceous chondrites:
897 Microtextures of a layered mineral containing Fe, S, O and Ni. *Geochim. Cosmochim. Acta* **49**, 2149-2163,
898 doi:10.1016/0016-7037(85)90073-0.

899 Tonui, E.K., Zolensky, M.E., Lipschutz, M.E., Wang, M.S. and Nakamura, T., 2003. Yamato 86029: Aqueously
900 altered and thermally metamorphosed CI-like chondrite with unusual textures. *Meteoritics Planet. Sci.* **38**, 69-
901 292, doi:10.1111/j.1945-5100.2003.tb00264.x.

902 Toppani, A., Libourel, G., Engrand, C. and Maurette, M., 2001. Experimental simulation of atmospheric entry of
903 micrometeorites. *Meteoritics Planet. Sci.* **36**, 1377-1396, doi:10.1111/j.1945-5100.2001.tb01831.x.

904 Trigo-Rodriguez, J.M., Rubin, A.E. and Wasson, J.T., 2006. Non-nebular origin of dark mantles around chondrules
905 and inclusions in CM chondrites. *Geochim. Cosmochim. Acta* **70**, 1271-1290, doi:10.1016/j.gca.2005.11.009.

906 van Ginneken, M., Folco, L., Cordier, C. and Rochette, P., 2012. Chondritic micrometeorites from the
907 Transantarctic Mountains. *Meteoritics Planet. Sci.* **47**, 228-247, doi: 10.1111/j.1945-5100.2011.01322.x

908 van Ginneken, M., Genge, M.J., Folco, L. and Harvey, R.P., 2016. The weathering of micrometeorites from the
909 Transantarctic Mountains. *Geochim. Cosmochim. Acta* **179**, 1-31, doi: 10.1016/j.gca.2015.11.045.

910 van Ginneken, M., Gattacceca, J., Rochette, P., Sonzogni, C., Alexandre, A., Vidal, V. and Genge, M.J., 2017. The
911 parent body controls on cosmic spherule texture: Evidence from the oxygen isotopic compositions of large
912 micrometeorites. *Geochim. Cosmochim. Acta*, doi:10.1016/j.gca.2017.05.008

913 Varela, M.E. and Kurat, G., 2009. Glasses in coarse-grained micrometeorites. *Earth Planet. Sci. Lett.* **284**, 208-
914 218, doi:10.1016/j.epsl.2009.04.030.

915 Velbel, M.A., Tonui, E.K. and Zolensky, M.E., 2012. Replacement of olivine by serpentine in the carbonaceous
916 chondrite Nogoya (CM2). *Geochim. Cosmochim. Acta* **87**, 117-135, doi:10.1016/j.gca.2012.03.016.

917 Wasson, J.T. and Rubin, A.E., 2014. Absence of matrix-like chondrule rims in CR2 LAP 02342. *Meteoritics Planet.*
918 *Sci.* **49**, 245-260, doi:10.1111/maps.12237.

919 Weisberg, M.K., McCoy, T.J. and Krot, A.N., 2006. Systematics and evaluation of meteorite classification. In
920 *Meteorites and the Early Solar System II*, D. S. Lauretta and H. Y. McSween Jr. (eds.), University of Arizona Press,
921 Tucson, 943:19-52.

922 Weisberg, M.K. and Huber, H., 2007. The GRO 95577 CR1 chondrite and hydration of the CR parent body.
923 *Meteoritics Planet. Sci.* **42**, 1495-1503, doi:10.1111/j.1945-5100.2007.tb00587.x

924 Welten, K.C., Folco, L., Nishiizumi, K., Caffee, M.W., Grimberg, A., Meier, M.M.M. and Kober, F., 2008. Meteoritic
 925 and bedrock constraints on the glacial history of Frontier Mountain in northern Victoria Land, Antarctica. *Earth*
 926 *Planet. Sci. Lett.* **270**, 308-315, doi:10.1016/j.epsl.2008.03.052.

927 Zolensky, M.E., Ivanov, A.V., Yang, S.V., Mittlefehldt, D.W. and Ohsumi, K., 1996. The Kaidun meteorite:
 928 Mineralogy of an unusual CM1 lithology. *Meteoritics Planet. Sci.* **31**, 484-493, doi:10.1111/j.1945-
 929 5100.1996.tb02090.x.

930 Zolensky, M.E., Mittlefehldt, D.W., Lipschutz, M.E., Wang, M.S., Clayton, R.N., Mayeda, T.K., Grady, M.M.,
 931 Pillinger, C. and David, B., 1997. CM chondrites exhibit the complete petrologic range from type 2 to 1: *Geochim.*
 932 *Cosmochim. Acta* **61**, 5099-5115, doi:10.1016/S0016-7037(97)00357-8.

933 Zolensky, M.E., Zega, T.J., Yano, H., Wirick, S., Westphal, A.J., Weisberg, M.K., Weber, I., Warren, J.L., Velbel,
 934 M.A., Tsuchiyama, A. and Tsou, P., 2006. Mineralogy and petrology of comet 81P/Wild 2 nucleus samples.
 935 *Science*, **314**, 1735-1739, doi:10.1126/science.1135842.

936 Zolensky, M., Mikouchi, T., Fries, M., Bodnar, R., Jenniskens, P., Yin, Q.Z., Hagiya, K., Ohsumi, K., Komatsu, M.,
 937 Colbert, M. and Hanna, R., 2014. Mineralogy and petrography of C asteroid regolith: The Sutter's Mill CM
 938 meteorite. *Meteoritics Planet. Sci.* **49**, 1997-2016, doi:10.1111/maps.12386.

939 Zolensky, M., Mikouchi, T., Hagiya, K., Ohsumi, K., Komatsu, M., Chan, Q.H., Le, L., Kring, D., Cato, M., Fagan,
 940 A.L. and Gross, J., 2016b. Unique View of C Asteroid Regolith from the Jbilet Winselwan CM Chondrite
 941 (abstract #2148) 46th Lunar and Planetary Science Conference. CD-ROM

942

943

944 **List of Tables and Figures:**

945 **Figure.1.** SEM-BEI data and element maps for TAM19B-7

946 **Figure.2.** SEM-BEI data and element maps for TAM19B-17

947 **Figure.3.** SEM-BEI data and elemental maps for TAM19B-18

948 **Figure.4.** SEM-BEI data for TAM15-11

949 **Figure.5.** SEM-BEI data and elemental maps for TAM66-1

950 **Figure.6.** Micrometeorite matrix geochemistry: spider diagram elemental abundance normalized to CI
 951 concentrations.

952 **Figure.7.** Micrometeorite matrix geochemistry: ternary diagram of major element composition

953 **Figure.8.** Micro-XRD patterns for 3 of the giant micrometeorites

954 **Figure.9.** Matrix geochemistry and inferred degree of alteration.

955 **Figure.10.** Estimated phyllosilicate fraction and inferred petrologic subtype, modified after Howard et al.,
 956 (2015).

957 **Figure.11.** 2D petrofabric analyses for the five micrometeorites

958 **Figure.12.** Examples of whole chondrules and a single chondrule **pseudomorph** from the small Antarctic
 959 micrometeorite populations.

960

961 **Table.1.** Analysis types collected on each micrometeorite.

962 **Table.2.** Geochemical data (WD-EMP and standard-based SEM-EDS spot analyses) collected from the particle
 963 matrix, anhydrous silicates, sulfides, CAIs and terrestrial alteration rims.

964 **Table.3.** Petrofabric analysis, circular statistics and entropy data.

965 **Table.S1.** Supplementary data file, uploaded as an excel file [not shown here] containing the bulk matrix
 966 geochemistry of 77 small, fine-grained Antarctic micrometeorites from the Cap Prud'homme collection. Data
 967 was used in Fig.9.

968

969 **Tables**

970 **Table.1.** Analysis types performed on each micrometeorite

Micrometeorite	Exposed surface area (mm ²)	BEI Exterior	BEI Interior	WD-EMPA [Cameca]	Standard-based EDS [Zeiss EVO]	Standard-less EDS [FEI Quanta 450]	EDX map [FEI Quanta 650/450]	μXRD	Fabric analysis	Phyllosilicate fraction
TAM19B-7	1.15		•	•	•	•	•	•	•	•
TAM19B-17	0.21		•	•			•	•	•	•
TAM19B-18	0.27		•	•	•		•	•	•	•
TAM15-11	0.30		•	•		•	•		•	•
TAM66-1	0.29	•	•	•		•	•		•	•

971

972

973

974

975

976

977 **Table.2.** (overleaf) Geochemical data from the five giant TAM micrometeorites. Data includes bulk matrix compositions, typical individual matrix analyses, analyses of
 978 altered CAIs, and anhydrous silicates. Data is shown in normalised wt%, although the uncorrected weight totals are also included for reference. Values quoted to 2 decimal
 979 places represent analyses collected on the WD-EMPA system, while analyses quotes to 1 decimal place represent data collected on an EDS system (black for standard-
 980 based and grey for standard-less). Elements with “*b.d.*” indicate values which are below detection limits. The location and suspected phase are included in the table and
 981 location data can be referenced against the spot locations shown in Figs.1-5.

No.	Particle	Analysis	N=	Al	Ca	Ti	Si	Mg	Fe	Ni	Cr	P	K	Na	S	O	Total	Total	FeO/SiO ₂	Mg# [At%]	Location
1	TAM19B-7	A0	51	2.8	0.1	<i>b.d.l</i>	22.0	2.3	26.6	0.5	0.7	0.2	1.0	0.6	3.1	40.2	100.0	83.5	0.74	18	Bulk
2	TAM19B-7	A1	1	3.4	<i>b.d.l</i>	<i>b.d.l</i>	19.0	4.4	28.7	<i>b.d.l</i>	0.6	<i>b.d.l</i>	0.5	0.0	3.5	40.0	100.0	73.0	0.91	26	Matrix analyses
3	TAM19B-7	A2	1	2.4	0.3	<i>b.d.l</i>	24.2	5.3	16.7	<i>b.d.l</i>	1.1	<i>b.d.l</i>	0.5	0.6	1.8	47.2	100.0	94.4	0.42	42	
4	TAM19B-7	A3	1	2.0	0.2	<i>b.d.l</i>	22.8	0.6	26.4	<i>b.d.l</i>	0.9	0.4	0.3	0.4	1.9	44.1	100.0	84.1	0.70	5	
5	TAM19B-7	A4	1	1.6	<i>b.d.l</i>	<i>b.d.l</i>	16.3	<i>b.d.l</i>	31.9	0.8	0.5	0.2	0.2	0.3	4.1	44.2	100.0	88.4	1.18	-	
6	TAM19B-17	B0	25	1.88	0.15	0.10	19.63	3.40	29.82	0.16	0.43	0.18	0.68	0.20	3.04	40.21	100.00	89.45	0.98	18	Bulk
7	TAM19B-17	B1	1	1.64	0.04	0.08	14.32	4.02	38.57	0.11	0.48	0.21	0.27	0.16	3.10	36.86	100.00	92.51	1.62	19	Matrix analyses
8	TAM19B-17	B2	1	1.87	0.20	0.11	26.87	0.72	23.57	0.07	0.48	0.24	0.59	0.22	1.83	43.17	100.00	81.94	0.53	7	
9	TAM19B-17	B3	1	2.26	0.06	0.06	15.96	7.89	33.39	0.11	0.23	0.03	0.06	0.12	1.72	37.90	100.00	98.58	1.26	35	
10	TAM19B-17	B4	1	3.7	6.8	0.2	20.7	6.0	16.8	<i>b.d.l</i>	0.5	0.1	0.6	0.6	1.9	42.0	100.0	101.8	0.5	45	
11	TAM19B-17	B5	1	5.1	0.3	0.1	16.1	7.1	29.5	0.1	<i>b.d.l</i>	0.1	0.3	0.6	1.5	39.0	100.0	87.6	1.1	36	Altered CAI edge
12	TAM19B-17	B6	1	1.8	7.9	<i>b.d.l</i>	26.9	10.8	5.7	<i>b.d.l</i>	0.4	<i>b.d.l</i>	<i>b.d.l</i>	<i>b.d.l</i>	0.8	45.6	100.0	104.7	0.1	81	Altered CAI other
13	TAM19B-18	C0	17	1.76	0.16	0.06	14.82	7.76	34.75	0.26	0.31	0.08	0.34	0.22	2.05	37.21	100.00	95.83	1.35	34	Bulk
14	TAM19B-18	C1	1	1.44	0.19	0.07	16.33	10.20	29.92	0.66	0.29	0.07	0.15	0.40	1.62	38.38	100.00	98.55	1.10	44	Matrix analyses
15	TAM19B-18	C2	1	1.57	0.10	0.05	14.90	7.77	36.30	0.12	0.31	0.02	0.14	0.13	1.62	36.72	100.00	96.94	1.47	33	
16	TAM19B-18	C3	1	1.77	0.36	0.06	16.03	6.63	33.99	0.27	0.29	0.05	0.08	0.13	2.24	37.89	100.00	98.94	1.28	31	
17	TAM19B-18	C4	3	1.59	0.24	0.08	18.67	9.11	26.10	0.39	0.50	0.14	0.22	0.36	2.11	40.23	100.00	95.29	0.84	44	
18	TAM19B-18	C5	1	2.5	0.1	<i>b.d.l</i>	23.7	2.7	22.1	0.2	0.4	<i>b.d.l</i>	0.3	<i>b.d.l</i>	3.7	43.4	100.0	80.7	0.56	22	Forsterite
19	TAM19B-18	C6	1	0.3	0.3	<i>b.d.l</i>	27.4	23.3	1.0	<i>b.d.l</i>	0.3	<i>b.d.l</i>	<i>b.d.l</i>	<i>b.d.l</i>	<i>b.d.l</i>	47.3	100.0	100.1	0.02	98	Forsterite
20	TAM15-11	D0	16	1.91	0.30	0.12	23.17	2.53	24.96	0.13	0.58	0.14	1.12	0.42	2.61	41.92	100.00	77.63	0.71	18	Bulk
21	TAM15-11	D1	1	2.41	0.19	0.12	34.24	2.15	11.11	0.04	0.59	0.04	0.48	0.29	0.73	47.56	100.00	73.07	0.20	31	Matrix analyses
22	TAM15-11	D2	1	2.48	0.17	0.13	29.22	2.77	18.03	0.19	0.66	0.17	0.43	0.37	0.74	44.56	100.00	87.41	0.37	26	
23	TAM15-11	D3	1	1.79	0.18	0.12	20.54	0.84	26.24	0.14	0.51	0.12	3.43	0.47	4.39	41.11	100.00	77.01	0.77	7	
24	TAM15-11	D4	1	20.43	0.13	0.02	3.13	0.17	23.33	0.05	0.21	0.10	4.41	0.07	7.24	40.63	100.00	86.02	4.49	2	
25	TAM15-11	D5	1	0.5	0.5	<i>b.d.l</i>	30.7	20.6	1.7	<i>b.d.l</i>	0.4	<i>b.d.l</i>	<i>b.d.l</i>	<i>b.d.l</i>	0.1	45.5	100.0	84.7	0.03	97	Low-Ca Px [En]
26	TAM15-11	D6	1	0.8	15.1	0.6	26.3	12.2	1.0	0.1	0.4	<i>b.d.l</i>	<i>b.d.l</i>	<i>b.d.l</i>	<i>b.d.l</i>	43.3	100.0	90.1	0.02	97	High-Ca Px [Aug]
27	TAM15-11	D7	1	1.9	15.0	0.4	25.3	10.0	2.4	<i>b.d.l</i>	1.5	<i>b.d.l</i>	<i>b.d.l</i>	<i>b.d.l</i>	<i>b.d.l</i>	42.7	100.0	86.7	0.06	91	High-Ca Px [Diop]
28	TAM15-11	D8	1	<i>b.d.l</i>	0.2	<i>b.d.l</i>	15.6	12.5	35.4	<i>b.d.l</i>	0.2	<i>b.d.l</i>	<i>b.d.l</i>	<i>b.d.l</i>	<i>b.d.l</i>	36.1	100.0	84.3	1.36	45	Fayalite
29	TAM66-1	B0	53	2.83	0.28	0.09	19.12	6.68	26.00	0.44	0.64	0.12	0.94	0.22	2.72	39.92	100.00	90.95	1.61	30	Bulk
30	TAM66-1	B1	1	2.86	0.16	0.06	16.88	8.70	25.91	0.54	0.19	0.03	1.22	0.48	3.60	39.37	100.00	94.35	0.83	37	Matrix analyses
31	TAM66-1	B2	1	1.94	0.31	0.10	19.19	10.31	24.34	0.63	0.42	0.12	0.12	0.27	2.00	40.25	100.00	93.24	0.92	44	
32	TAM66-1	B3	1	1.66	0.05	0.07	13.74	7.00	36.66	4.00	0.13	0.05	0.06	0.03	1.48	35.08	100.00	104.67	0.76	49	
33	TAM66-1	B4	1	2.77	0.41	0.08	15.07	8.90	28.72	0.42	0.28	0.15	1.33	0.31	3.37	38.18	100.00	92.64	1.15	42	
34	TAM66-1	B5	1	3.75	0.26	0.09	17.53	6.20	25.91	0.30	0.30	0.09	1.74	0.37	3.82	39.65	100.00	89.80	0.89	35	Fine-grained rim analyses
35	TAM66-1	B6	1	3.42	0.24	0.09	15.75	7.43	29.05	0.29	0.21	0.10	1.36	0.17	3.42	38.46	100.00	92.17	1.11	37	
36	TAM66-1	B7	1	2.32	0.08	0.15	22.11	2.75	25.54	0.14	1.88	0.03	1.17	0.22	2.91	40.70	100.00	78.42	0.69	20	Altered chondrules
37	TAM66-1	B8	1	3.03	0.07	0.16	27.16	1.43	20.73	0.28	1.86	0.08	0.66	0.11	1.27	43.17	100.00	74.35	0.46	14	Low-Ca Px [En]
38	TAM66-1	B9	1	<i>b.d.l</i>	0.3	<i>b.d.l</i>	20.6	20.6	25.5	0.2	0.3	<i>b.d.l</i>	<i>b.d.l</i>	<i>b.d.l</i>	<i>b.d.l</i>	32.5	100.0	82.5	0.74	65	
39	TAM66-1	B10	1	1.50	8.69	0.24	23.16	12.62	8.79	0.06	0.51	0.07	0.26	0.01	0.74	43.36	100.00	97.94	0.23	77	High-Ca Px [Aug]
40	TAM66-1	B11	1	0.01	0.11	0.01	16.96	18.33	25.10	0.05	0.25	0.01	0.00	0.03	0.00	38.87	100.00	101.26	0.89	63	Fayalite
41	TAM66-1	B12	1	36.19	0.23	0.15	0.57	16.41	1.27	0.04	0.44	0.01	0.03	0.02	0.04	44.60	100.00	96.38	1.32	97	Mg-Al Spinel
42	TAM66-1	B13	1	36.8	<i>b.d.l</i>	0.4	0.8	16.8	3.2	<i>b.d.l</i>	3.5	<i>b.d.l</i>	0.1	<i>b.d.l</i>	<i>b.d.l</i>	38.6	100.0	80.4	2.46	92	

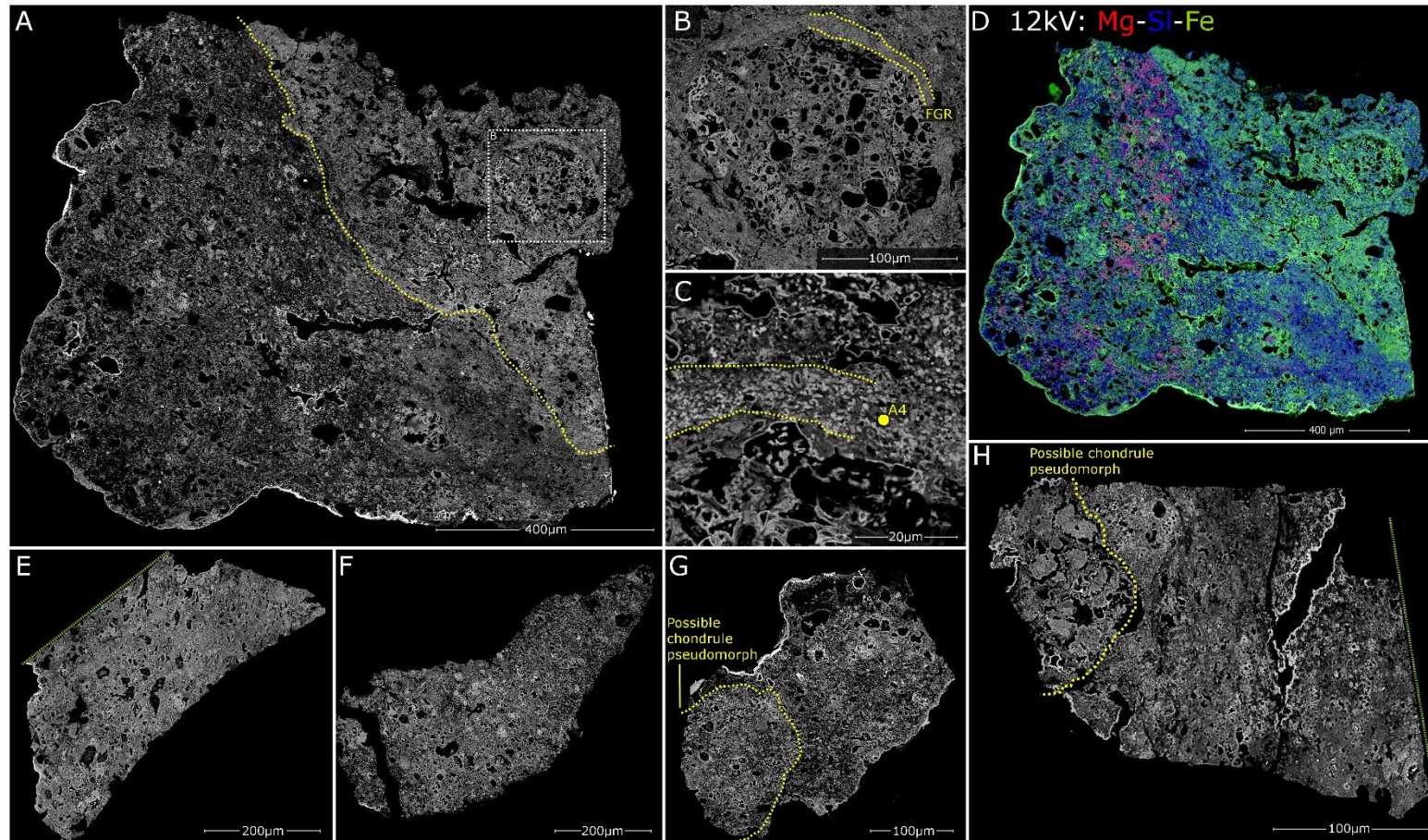
983 **Table.3.** Petrofabric analysis, circular statistics and entropy results.

No.	Sample	N=?	No. of fabrics	Entropy (S)	S<S _{cutoff}	Circ. Var	Circ. Kurtosis	Circ. Std. Dev.	Kappa (κ)
1	TAM19B-7	445	1	2.599	Positive	0.18	-11.25	36.41	1
2	TAM19B-17	48	1	2.688	Positive	0.24	-4.81	42.88	0.69
3	TAM19B-18	309	1	2.785	<i>Possible</i>	0.26	-3.84	44.61	0.62
4	TAM15-11	329	2	2.744	<i>Probable</i>	0.36	-1.73	54.56	0.33
5	TAM66-1	516	1	2.860	Negative	0.48	-0.28	65.36	0.15
6	Cold Bokkeveld	1054	1	2.619	<i>Reference value</i>	0.23	0.32	41.43	0.75
7	Jbilet Winsewlan	950	2	2.783	<i>Threshold value</i>	0.44	0.36	61.52	0.2

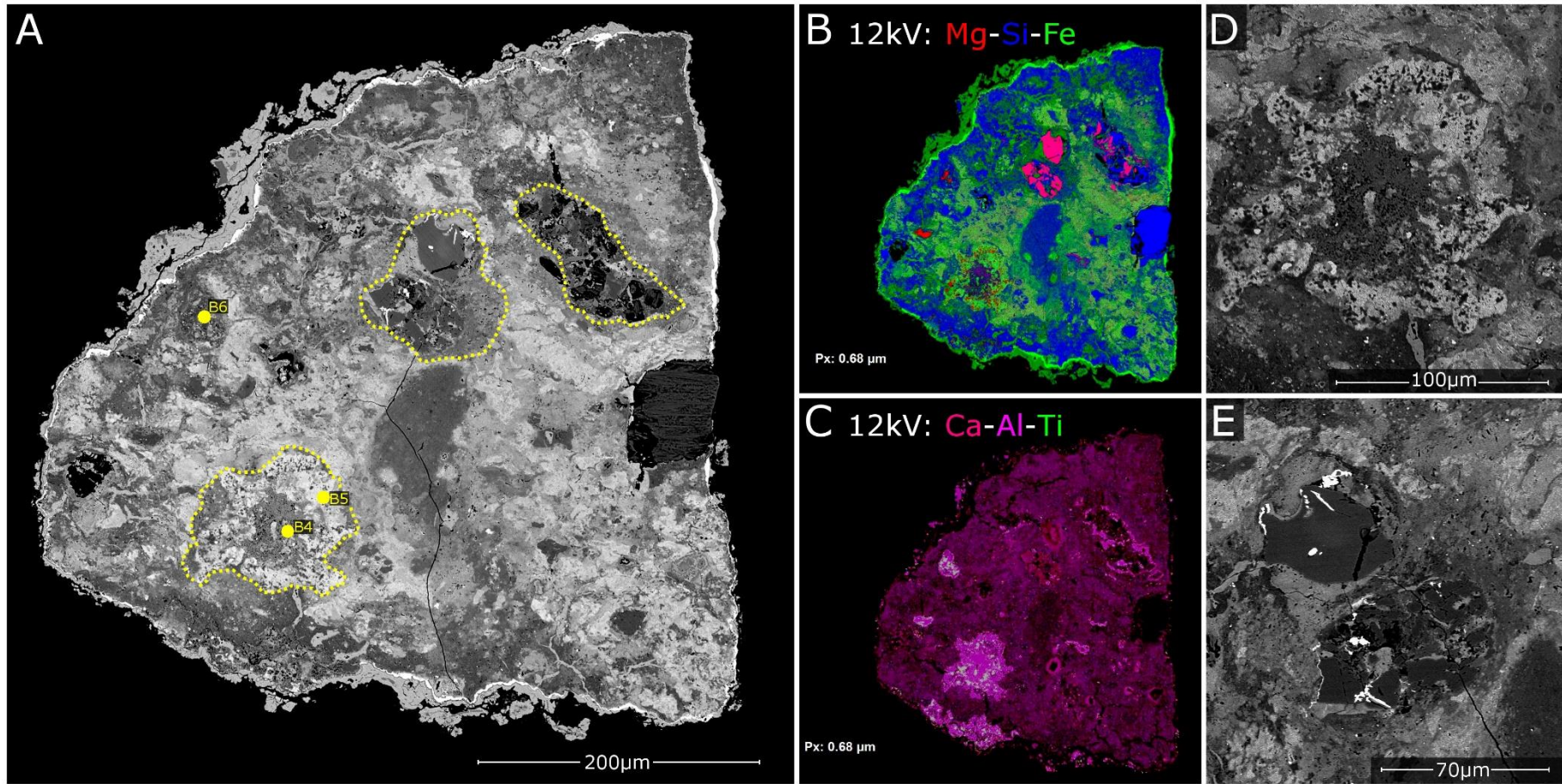
984

985 **Figure.1.** A) Particle TAM19B-7, a giant fine-grained micrometeorite. This figure displays both the primary cross-sectioned view (A-D, 830x950 μ m) and slices through
986 additional fragments produced after the particle was crushed (E-H). The main cross-section (A-D) shows a well-defined geochemical boundary, separating two zones of
987 distinct matrix, the larger “left hand” zone is Mg-bearing (4.1-8.2wt%), while the “right hand” portion is Mg depleted, with Mg concentrations below 3.0wt%. This region
988 contains a circular inclusion, interpreted as a chondrule pseudomorph and highlighted by a dashed white square (B). The inclusion has a high porosity and is composed of
989 phyllosilicate decomposition products. Its elliptical shape could indicate compaction during impact. There is also a compact, fine-grained rim [FGR] (C), approximately 15 μ m
990 thick and containing Fe-Ni oxide nuggets surrounds the inclusion. The yellow A4 symbol denotes the position of a spot EDS analysis, shown in Table.2. A major element (Mg,
991 Si, Fe) EDX map is shown in (D). In contrast, E-H show additional fragments, revealing a paucity of coarse-grained components throughout the particle. In H we have highlighted
992 the tentative outline of a second possible pseudomorph chondrule, similar to that shown in B and C. The stippled green lines in E and H mark where the initial cross-section
993 cut through the particle.

994
995
996



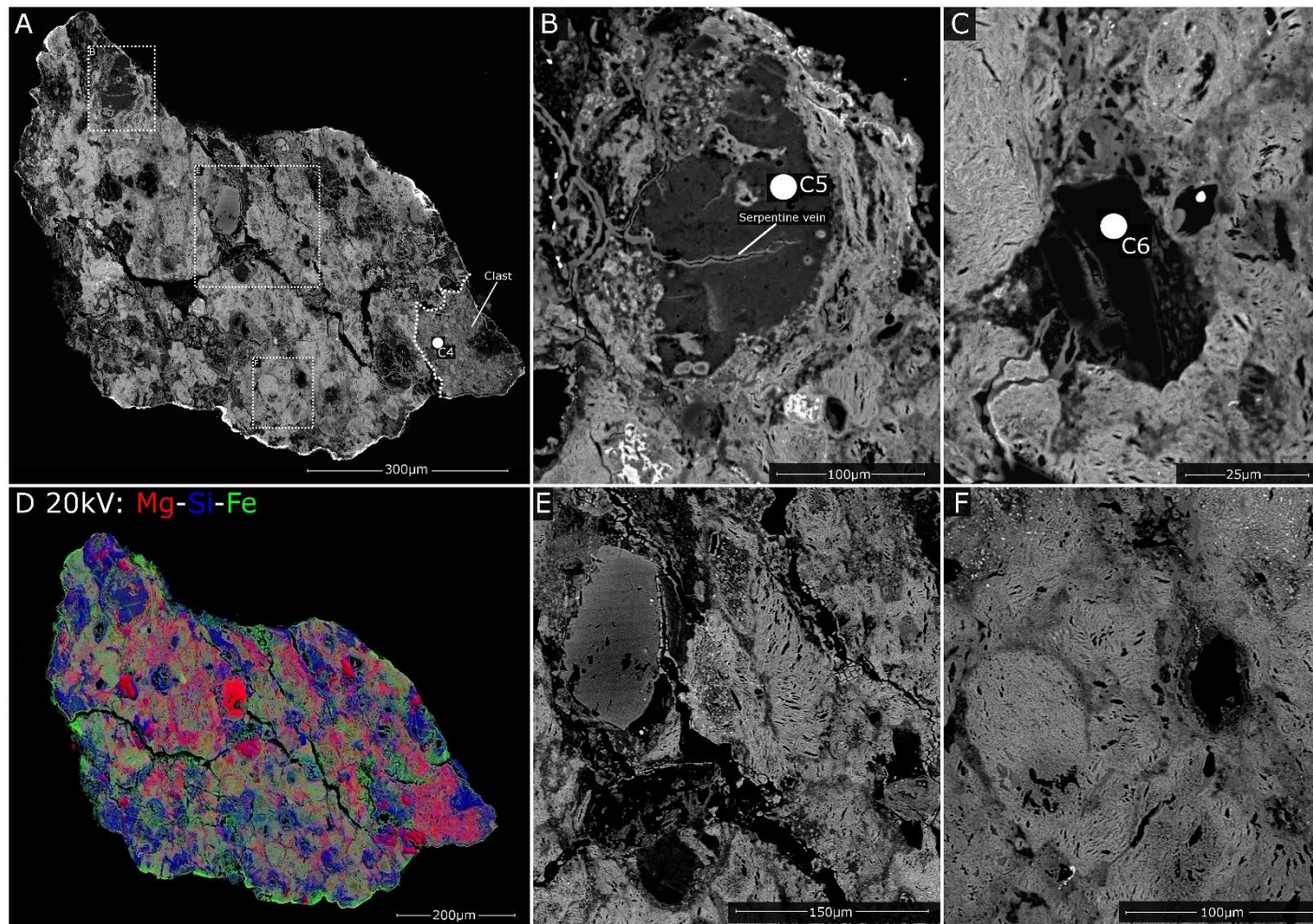
997 **Figure.2.** A) Particle TAM19B-17, this micrometeorite has a triangular cross-section and contains a compact, low-porosity and intensely aqueous altered internal texture. A
998 thick jarosite encrustation rim surrounds the particle attesting to a significant period of terrestrial weathering. Inside the weathering encrustation is a magnetite rim, produced
999 by atmospheric entry heating. The matrix contains a complex intermix of lighter (Fe-rich) and darker (Mg-rich) zones that are intergrown and cross cut by later periods of
1000 veining and pore-filling. Three regions are highlighted by a dashed yellow line, these indicate where refractory phases (silicates and oxides) have been partially altered and
1001 replaced, these zones are interpreted as ghost CAIs. Yellow dots B4-6 denote the locations of EDS spot analyses, shown in Table.2. Element maps (B and C) reveal the major
1002 element and trace refractory element distributions, and these aid in the identification of hydrated and partially replaced CAIs (D) and altered isolated anhydrous silicates (E).



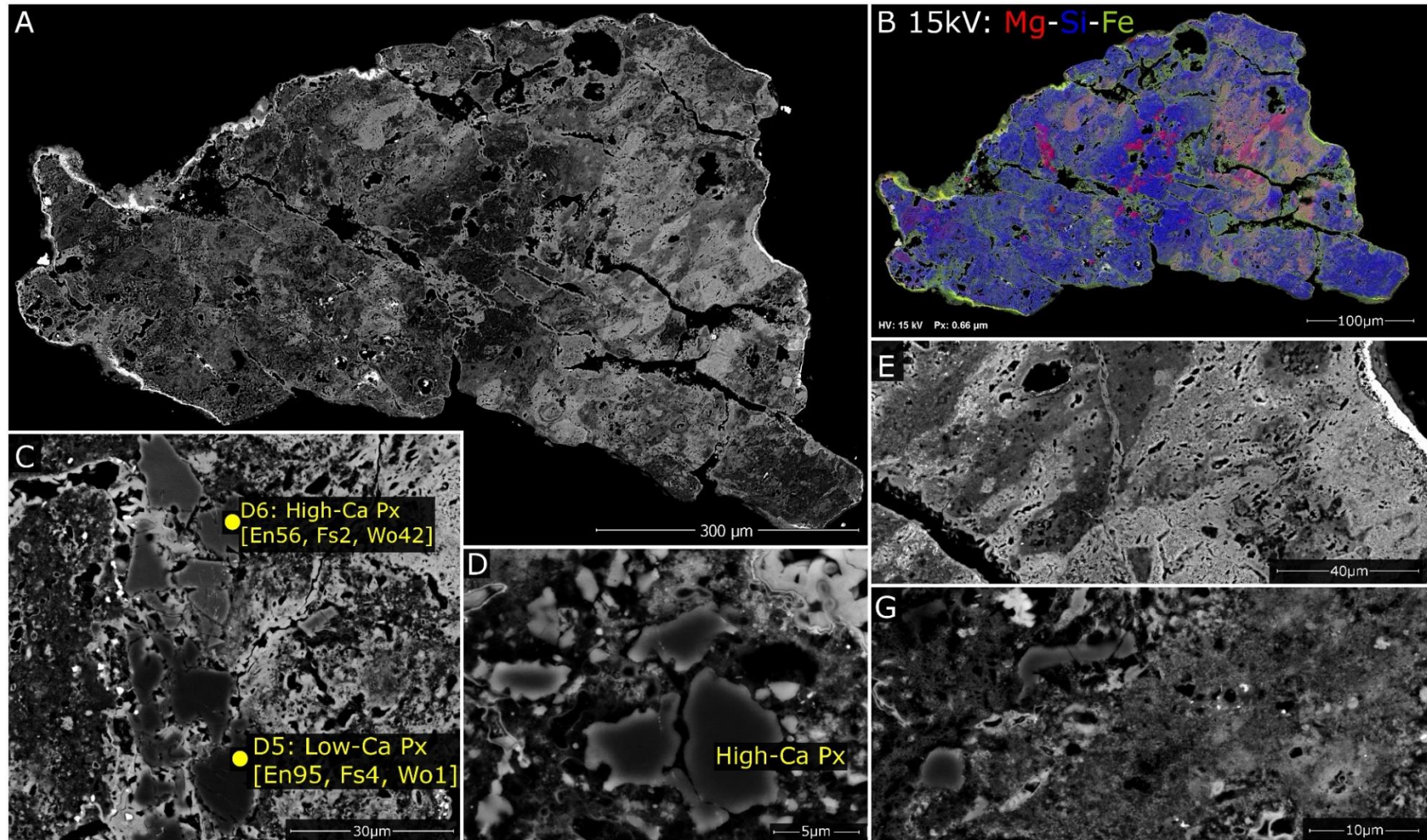
1003 **Figure.3.** A) Particle TAM19B-18. This micrometeorite is composed of >85% matrix and is dominated by coarse, Fe-rich phyllosilicate decomposition products, which prior to
1004 atmospheric entry would have been cronstedtite (serpentine) clusters - equivalent to the PCP clumps described in previous studies of CM chondrites (Rubin et al., 2007). A
1005 lithic clast, composed of compact, Mg-rich matrix and containing a single large olivine crystal is found in the bottom right corner. The symbol C4-6 denote the location of an
1006 EDS spot analyses, shown in Table.1. (B, C, D and E) Anhydrous silicates are relatively rare and have anhedral rounded morphologies, containing abundant fractures, filled
1007 with serpentine alteration products, or are broken into a series of smaller, rounded and residual crystal relicts. Large phyllosilicate overgrowths mantle most grains, and in
1008 places generate a foliation texture, wrapping around larger crystals. Note: the view shown in (C) is from a higher plane of section and, therefore, cannot be located on the
1009 whole particle image, seen in (A). A major element (Mg, Si, Fe) EDX map is shown in (D).

1010

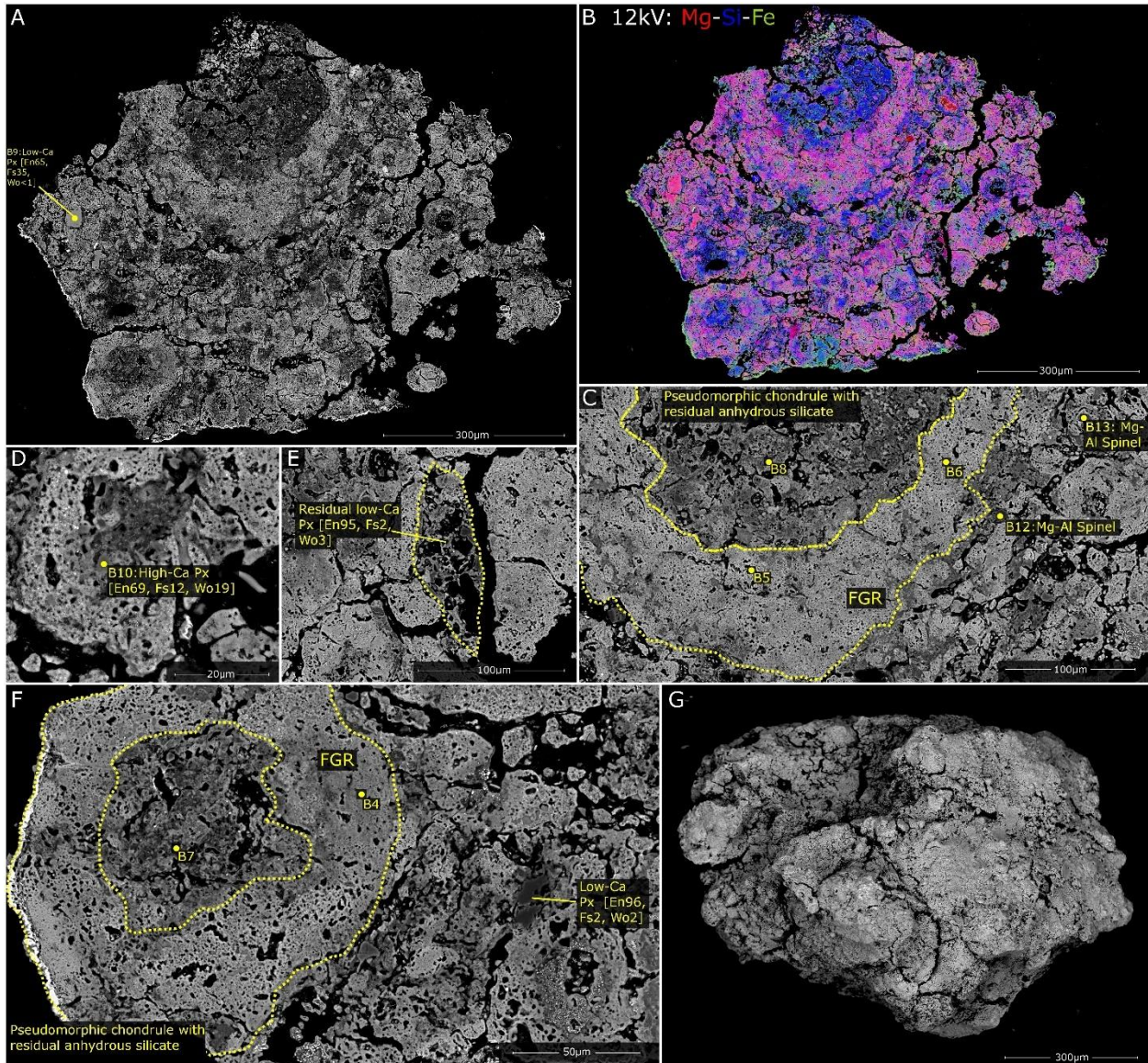
1011



1012 **Figure.4.** A) Particle TAM15-11 This micrometeorite has a broadly triangular cross-section, with a prominent magnetite rim. The internal mineralogy is dominated by
1013 (dehydroxylated) Fe-rich phyllosilicate. The right side of the particle (E) contains primarily coarse-grained phyllosilicate clusters with lozenge shapes,
1014 while the left side of the particle (G) is finer-grained, contains more Mg and preserves some fractured anhydrous silicate crystal relicts with low and high-Ca pyroxene compositions (C and D). The
1015 major element EDX map (B) demonstrates that the entire particle is Mg-poor, most likely reflecting the action of leaching during terrestrial weathering.
1016

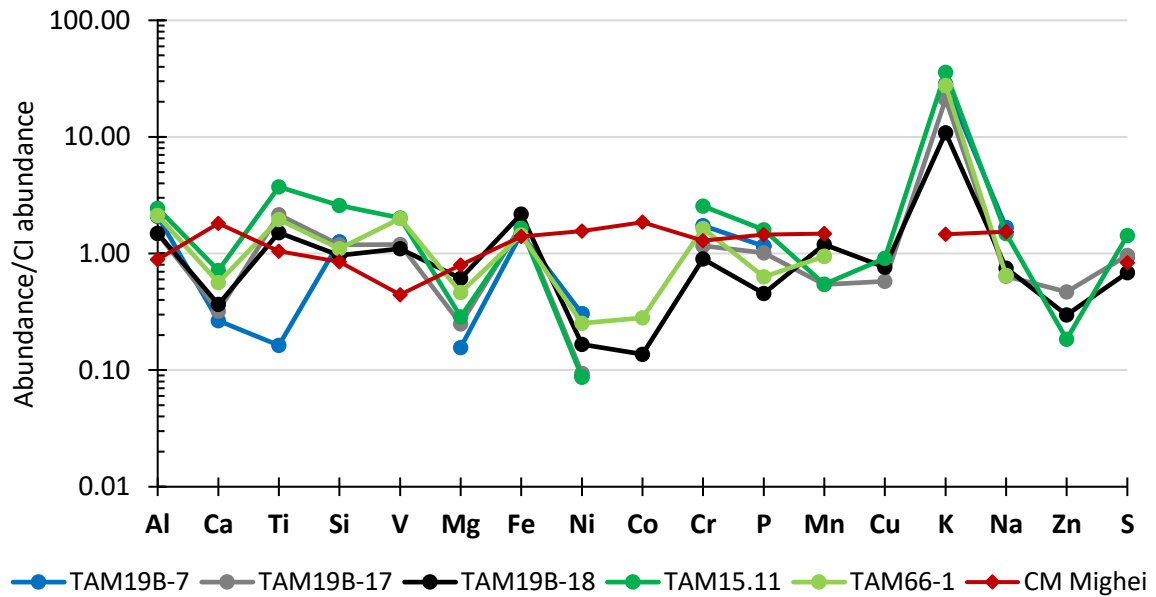


1017 **Figure.5.** A) Particle TAM66-1, this micrometeorite is composed of Fe-rich vesicular matrix surrounding regions
 1018 of darker, fine-grained Fe and Mg-poor matrix, as shown in the major element EDX map (B). In addition to the
 1019 two large and approximately circular inclusions, which are easily distinguished and shown in C and F, several
 1020 smaller zones of dark matrix are also surrounded by vesicular Fe-rich matrix, as shown in D and E. We interpret
 1021 these circular regions as altered pseudomorphic chondrules, which originally had thick fine-grained rims (FGR).
 1022 In contrast, the smaller dark inclusions represent phyllosilicate growth around isolated anhydrous silicate
 1023 crystals and subsequent (partial) replacement. This particle texture, therefore, closely resembles the matrix of
 1024 an intensely altered CM chondrites.



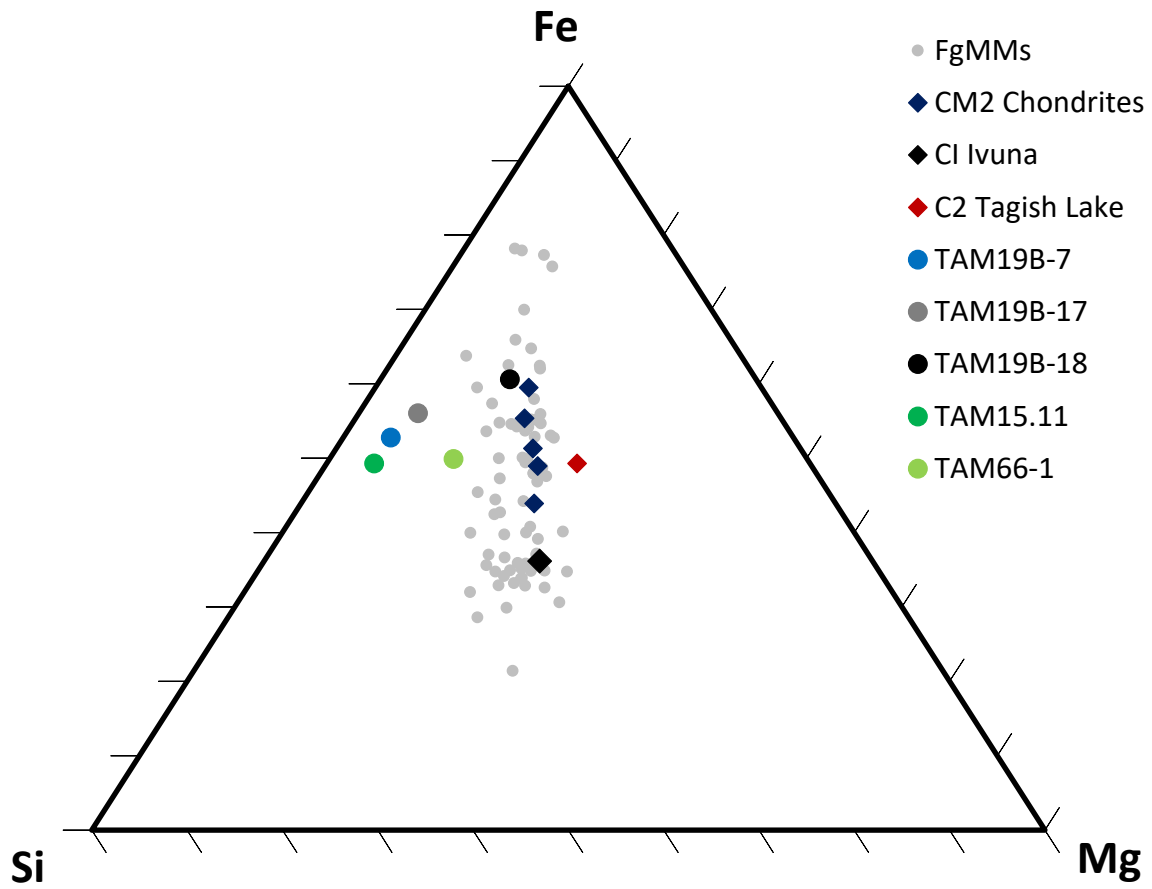
1025

1026 **Figure.6.** Micrometeorite matrix geochemistry: spider diagram showing elemental abundances for the five giant
 1027 micrometeorites (TAM19B-18 [green], TAM19B-18 [black], TAM19B-7 [blue], TAM15-11 [dark green] and
 1028 TAM66-1 [light green]) and the CM chondrite Mighei (a fresh fall) for reference. Elements are ordered by
 1029 decreasing volatility, as defined by Lodders (2003) and normalized against CI carbonaceous chondrite values,
 1030 obtained by analysis on a chip of Ivuna. These samples show a common abundance pattern, characteristic of the
 1031 TAM micrometeorites. Samples are chondritic but with notable depletions in Ca (0.27-0.72), Mg (0.16-0.61), Ni
 1032 (0.09-0.31), Co (b.d.l-0.28), Cu (b.d.l-0.91) and Zn (b.d.l-0.47). Meanwhile, particles are also significantly elevated
 1033 in K, with concentrations between 10-25 times CI values. This pattern of depletions and enrichments is
 1034 characteristic of the TAM micrometeorites and traces the effects of subaerial Antarctic terrestrial weathering on
 1035 a chondritic sample (van Ginneken et al., 2016; Suttle et al., 2018).



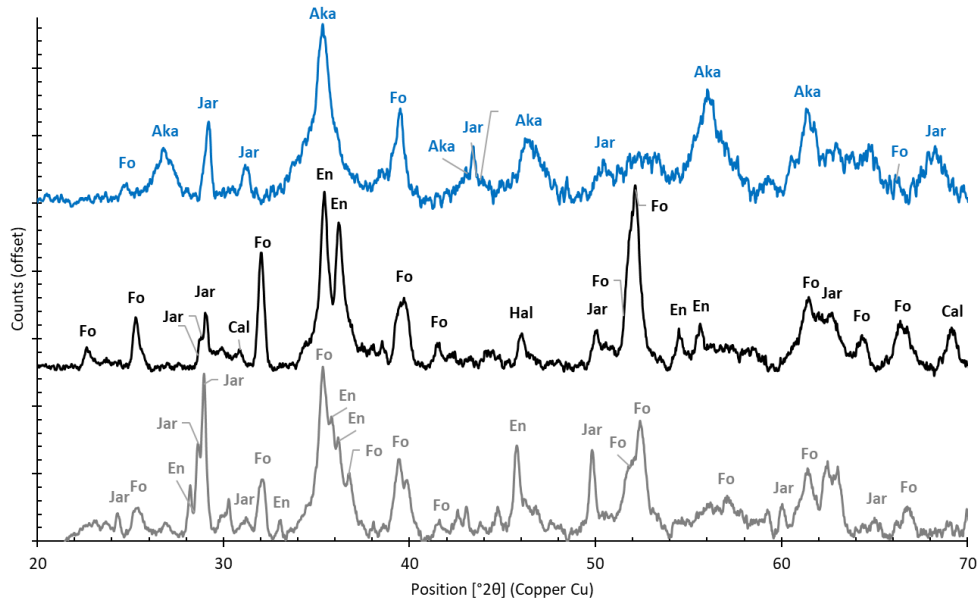
1037 **Figure.7.** Micrometeorite matrix geochemistry: ternary diagram showing major element (Mg-Fe-Si) abundance
1038 relative to a population of 77 small fine-grained micrometeorites from the Cap Prud'homme collection and
1039 several reference hydrated carbonaceous chondrites.

1040

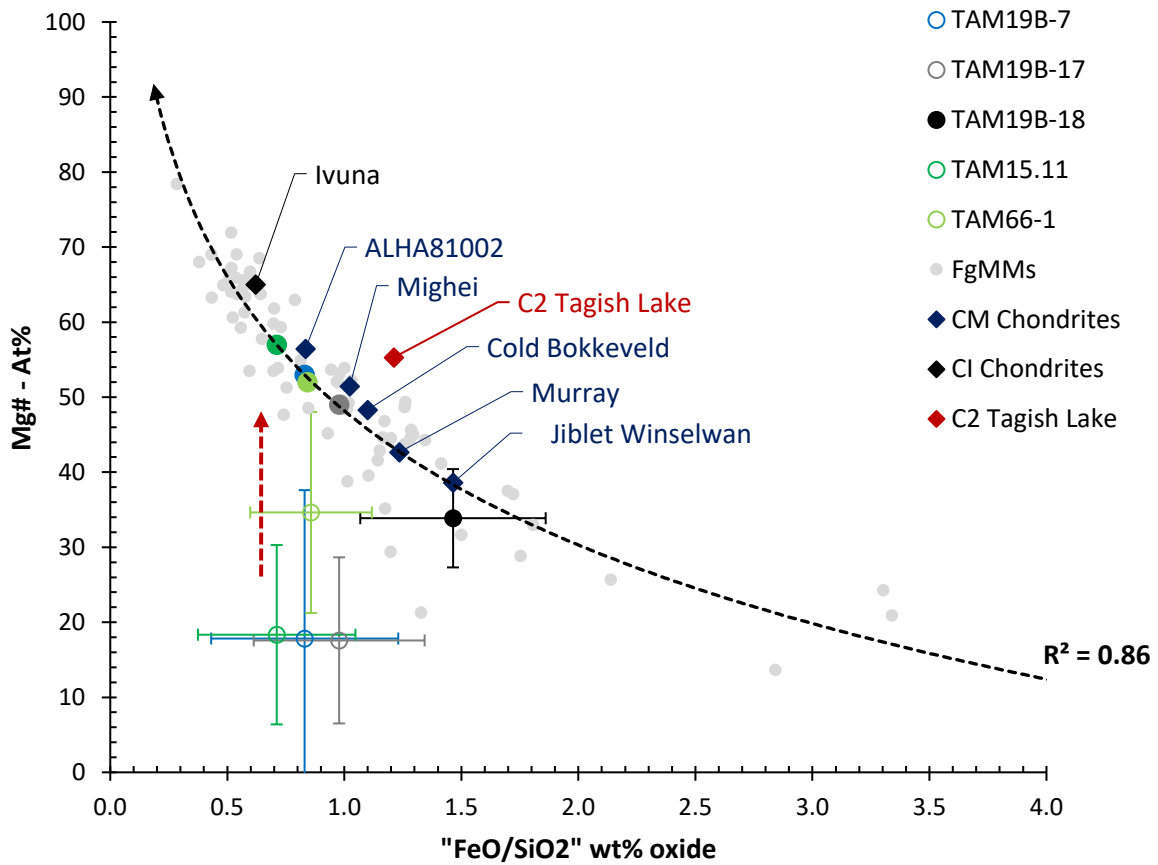


1041 **Figure.8.** Micro-XRD patterns from TAM19B-17 (grey), TAM19B-18 (black) and TAM19B-7 (blue). Patterns are
1042 offset to aid interpretation. Major peaks associated with each mineral are marked using the following standard
1043 abbreviations: Fo=forsterite, En=enstatite, Aka=akaganéite, Cal=calcite, Hal=halite and Jar=jarosite. The last four
1044 minerals (Aka, Cal, Hal and Jar) are terrestrial weathering products, however, the presence of akaganéite implies
1045 the former existence of troilite and pyrrhotite, extraterrestrial Fe-Ni sulfide minerals. As with the spider
1046 diagrams, these XRD patterns are characteristic of TAM micrometeorites.

1047
1048
1049
1050



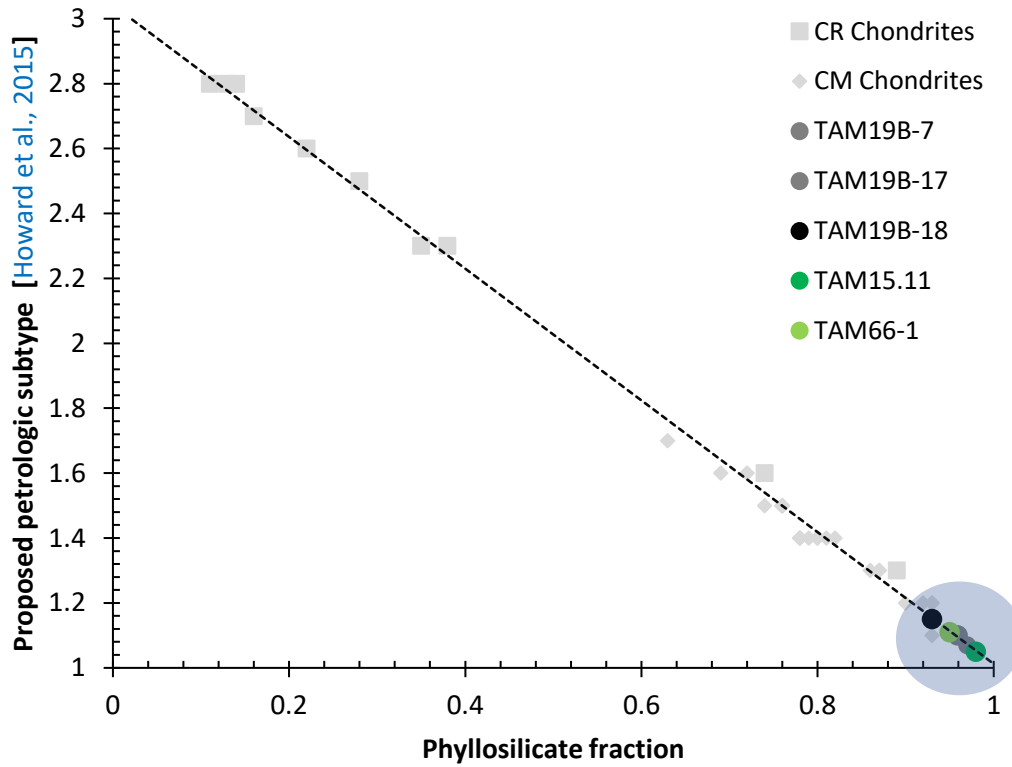
1051 **Figure.9.** Micrometeorite matrix geochemistry (FeO/SiO₂ [wt%] vs. Mg# [At%]) and inferred degree of alteration.
 1052 This chart uses two separate geochemical metrics to evaluate the degree of aqueous alteration in a hydrated
 1053 chondritic sample. The bulk matrix compositions of 77 small fine-grained Antarctic micrometeorites (FgMMs)
 1054 from the Cap Prud'homme collection (previously analyses in Suttle et al. [2017a]) are used as a reference
 1055 values to define an "aqueous alteration trendline", calculated as a logarithmic linear regression line (R²=0.86).
 1056 Reference values from several CM chondrites, the CI chondrite Ivuna and the ungrouped meteorite C2 Tagish
 1057 Lake are also shown. The matrix compositions for the five giant micrometeorites are also plotted. Four are shown
 1058 as coloured open circles; these particles have anomalously low Mg values, which do not plot along the alteration
 1059 trendline, suggesting they have experienced a later episode of Mg depletion. This is interpreted as the effect of
 1060 terrestrial weathering leading to the leaching of Mg and is a common occurrence in micrometeorites with long
 1061 terrestrial residence times (Kurat et al., 1994; van Ginneken et al., 2016). Their corrected Mg# values are shown
 1062 as large solid coloured circles. Corrected values are calculated simply by raising their Mg# value until each
 1063 micrometeorite lies directly on the alteration trendline (dashed red arrow). The TAM micrometeorites,
 1064 therefore, span a range of alteration degrees reflecting a similar range to the well-studied CM chondrites (Jbilet
 1065 Winselwan to ALHA 81002). Error bars show 1 standard deviation from the micrometeorite's average matrix
 1066 composition.



1067
 1068
 1069

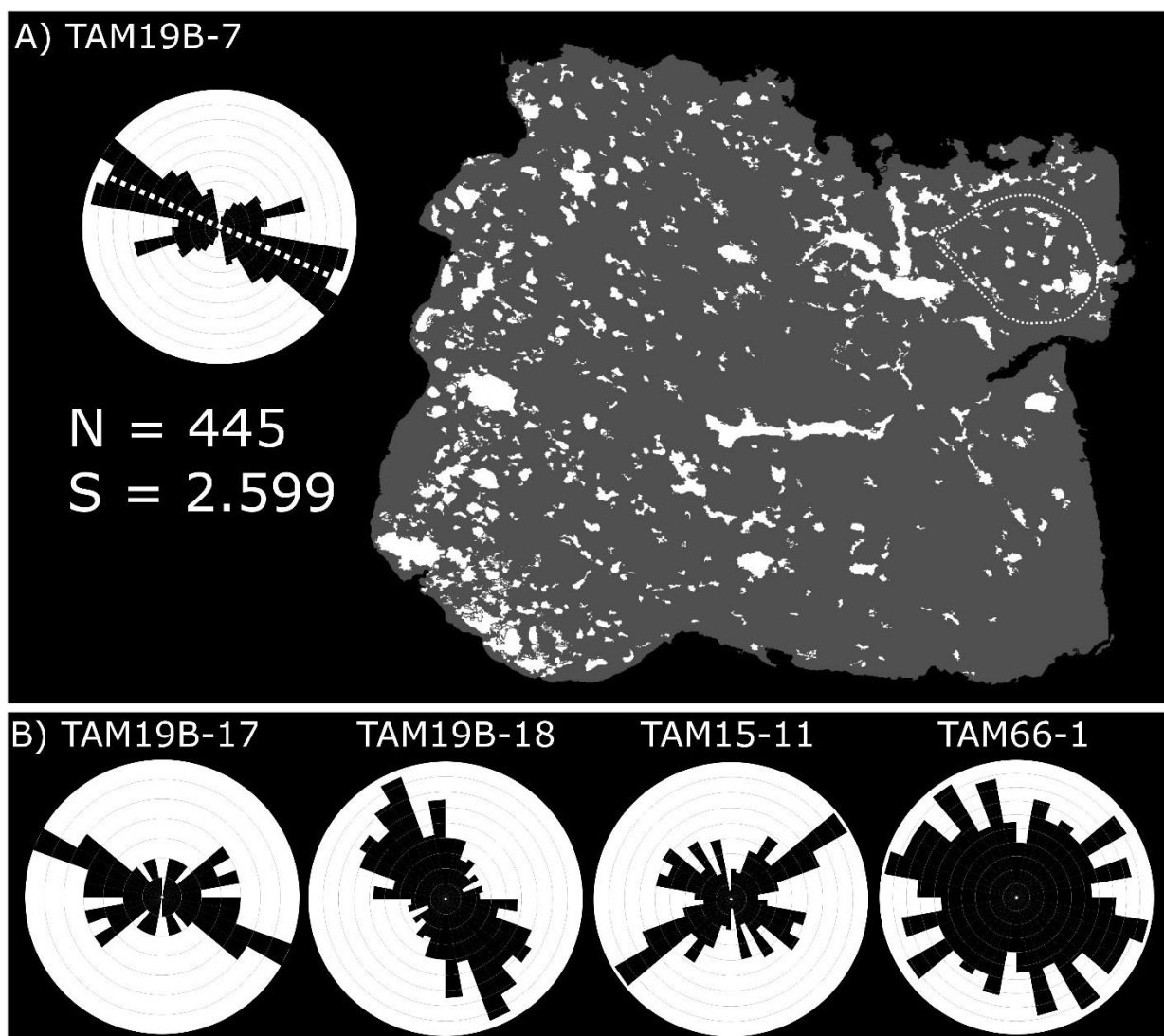
1070 **Figure.10.** Estimated phyllosilicate fraction and inferred petrologic subtype, modified after Howard et al., (2015)
1071 using data from CM, CR and ungrouped C2 chondrites. The five TAM micrometeorites (circled)
1072 have high phyllosilicate fractions (93-98%) suggesting low petrologic subtypes (<1.2) and, thus, intense alteration.

1073



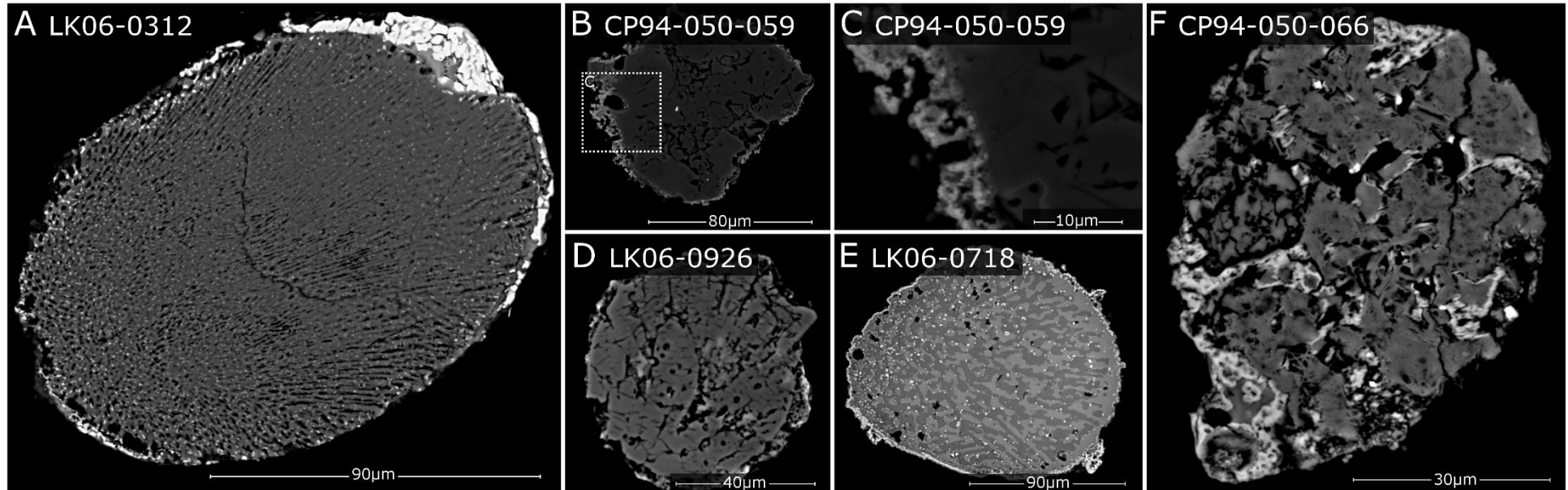
1082 **Figure.11.** Petrofabric analysis, based on void orientations, using the method outlined in Suttle et al., (2017b).
1083 Voids were extracted from the BEI data and their orientation (long-axis) with respect to an arbitrary “north”
1084 recorded. A rose diagram of the void orientations (binned by 10° increments) was plotted and used to evaluate
1085 the presence or absence of a petrofabric. A strong uniaxial fabric is seen in TAM19B-7, this is also parallel to the
1086 elongation axis of the chondrule (shown by the dashed white line in the rose) suggesting both the matrix and
1087 chondrule are deformed in the same event, most likely an impact. Rose diagrams for the other four
1088 micrometeorites are also shown, three of which show evidence for a uniaxial fabric.

1089



1090

1091 **Figure.12.** Complete chondrules, chondrule fragments and a single chondrule pseudomorph previously identified among the (small, <<400 μ m) Antarctic micrometeorite flux.
1092 These particles were collected from either Cap Prud'homme [CP94-] or Larkman Nunatak [LK06-]. Particles LK06-0312 (A), LK06-0926 (D) and LK06-0718 (E) are single crystal,
1093 radiating pyroxene chondrules, while CP94-50-059 (B and C) is a composite micrometeorite, composed of an anhydrous olivine crystal mantled by fine-grained matrix, which
1094 subsequently melted during atmospheric entry, forming a thin igneous rim (Genge et al., 2005; Genge, 2006). CP94-050-066 (F) is interpreted as an (unmelted) chondrule
1095 pseudomorph, whose pre-atmospheric mineralogy was intermixed phyllosilicate and tochilinite that later thermally decomposed during entry heating.



Source file

[Click here to download Source or Other Companion File: Revised_manuscript.docx](#)

Supplementary file Table.S1

[Click here to download Source or Other Companion File: Table.S1.xlsx](#)

Associated MAPS manuscript, requested for reference

[Click here to download Source or Other Companion File: Atmospheric_entry_frag_manuscript_MAPS.pdf](#)